Unstable Folding of Lithospheres: Constraining the Thermal History of a Planetary Body

By

JONATHAN KAY
B.A., Wheaton College (MA), 2008
M.S., University of Idaho, 2010

THESIS

Submitted as partial fulfillment of the requirements
for the degree of Doctor of Philosophy in Earth and Environmental Sciences in the Graduate
College of the
University of Illinois at Chicago, 2017

Chicago, Illinois

Defense Committee:

Andrew Dombard (Chair Earth and Environmental Sciences, UIC)

Roy Plotnick (Earth and Environmental Sciences, UIC)

Stefany Sit (Earth and Environmental Sciences, UIC)

Carol Stein (Earth and Environmental Sciences, UIC)

DEDICATION

To my beautiful and wonderful wife for always supporting me.
To my amazing son for always bringing a smile to my face.

ACKNOWLEDGMENTS

This work would not have been possible without the help of Andrew Dombard, my mentor and advisor for his support, nurturing, and guidance through these years.

To Roy Plotnick, Stefany Sit, and Carol Stein for always having their doors open for any question I could have.

To Minnie, Edna, and Dr. Nagy for keeping this place running and me focused.

To NASA for funding me to do what I love.

To my extended family for helping me get here.

To Dr. Steve Hauck for sharing access to his server at Case Western Reserve University.

CONTRIBUTIONS OF AUTHORS

As part of this work I have prepared chapters II, III, and IV to represent manuscripts that I am the primary author of and have done the modeling and analysis. These works have been formatted in preparation for submission in the journal *Icarus*. Dr. Andrew J. Dombard mentored me through this process of research and contributed to all three manuscripts.

PREFACE

The motivation behind these studies is to understand better the thermal and structural history of the lithospheres of three bodies in the solar system by examining a common physical process expressed at three different scales (global, regional, and local). The formatting of this work is that each chapter are in the form of a manuscript, each of which will ultimately be submitted to the journal *Icarus* for publication. Each chapter represents unique research, but Chapter III and IV are based on the methodology discussed at length in Chapter II. Nevertheless, there is some redundancy in the presentation of the methodology, sufficient to allow each chapter to exist as a stand-alone paper.

To summarize, Chapter I is a brief discussion of the work in this Thesis. Chapter II is a detailed look at the thermal and mechanical history of the formation of the oblate shape on Saturn’s moon Iapetus. Chapter III presents work attempting to explain the existence of long-wavelength topography on Mercury using an elastic-viscous-plastic rheology. Last, Chapter IV explores the formation of short wavelength features on Saturn’s moon Enceladus using an elastic-viscous-plastic rheology.

TABLE OF CONTENTS

LIST OF FIGURES

CHAPTER PAGE

CHAPTER II

CHAPTER III

LIST OF TABLES

CHAPTER I

I. INTRODUCTION

A. **Background**

My graduate work focused on understanding the relationship of folding of planetary lithospheres (the mechanically stiff outer layer of a planetary body) on a variety of length scales using an elastic-viscous-plastic rheology, which lowers the stress requirements for deformation to occur over models with more simplistic (and thus less realistic) rheological models (e.g., a purely elastic lithosphere). The surfaces of planetary bodies record the structural and tectonic histories, the styles of which are mostly strongly controlled by heat flow. This phenomenon is best exemplified by long term retention of impact craters. On bodies such as the Moon that have no atmosphere, low heat flow, and no other sources of erosion, impact craters are preserved for perpetuity or until another crater forms on top. This observation is compared to Jupiter's moon Ganymede that is also saturated with craters, but the craters can be age-identified by their state of preservation. Older craters have become flattened and have 'relaxed' due to a long-term low heat flow that causes the material supporting the topography of the crater to flow away slowly. I have extended this type of work to three projects across the solar system, and have incorporated unstable contractional deformation (i.e., folding). I have used this numerical modeling technique to explain three sets of potentially folded features: the oblate shape of Saturn's moon Iapetus (that is, folding on a global scale), the observed long wavelength topography near the Caloris Basin on Mercury (regional scale), and periodic topography within and bounding the South Polar Terrain on Saturn's moon Enceladus (local scale).

B. Unstable Deformation and the Formation of the Equatorial Bulge of Iapetus

My work on Saturn's moon Iapetus sought to test if it was possible to form the distinctly oblate shape of Iapetus through folding of the lithosphere during an epoch of global contraction. Presently, the difference between the equatorial radius and polar radius is ~35.0 km, yielding a flattening of ~5%. Previous models that attempted to explain the formation of the pronounced oblate shape of Iapetus suggested that it was a preserved rotational bulge. These models assumed that the heating was provided by short-lived radioactive isotopes that decayed rapidly and allowed the excess flattening of the lithosphere to be locked in by a thickening lithosphere, but placed severe timing constraints on the formation of Iapetus and its bulge. My work showed that it was possible to form the oblate shape through long-wavelength folding of the lithosphere during an epoch of contraction, where 10% of strain occurred, that was combined with a latitudinal surface temperature variation. The simulations that were most effective at reproducing the observed shape occurred when the temperature variation approached 30 K, and these simulations produced approximately 45 km of radial difference, which exceeds the presently observed amount. My results have provided an alternative formation mechanism for the bulge, one that is not hampered by the severe timing constraints placed on it by the rotational models.

C. A Test for Developing Long-Wavelength Lithospheric Folding on Mercury

Next, I wanted to test the limitation on the amount of strain required to induce folding of the lithosphere. Mercury is the right body for this work because the surface of Mercury is covered with contractional tectonic features (e.g., lobate scarps). The lobate scarps are believed to be the surface expression of large thrust faults that resulted from the contraction of the lithosphere due to the cooling of the planet. The scarps have formed by an estimated 1-15 km of radial contraction (equivalent to ~0.6% of horizontal shortening) that postdates the late heavy bombardment ~3.9-4.0 Ga, suggesting that there have not been any global resurfacing events since then. Another, more subtle consequence of global contraction may have been the formation of long-wavelength, low-amplitude topography. This type of topography has been predicted to exist on Mercury; however, it was not until the MESSENGER (MErcury Surface, Space ENvironment, GEochemistry, and Ranging) spacecraft began collecting data from Mercury that the existence of long-wavelength topography was identified. The Caloris impact basin showed that the smooth plains interior to the basin rim display long-wavelength variations in topography, while other broad swells exist outside the basin that roughly follow the same trend line. To test the wavelength at which these structures would grow most quickly, I built multiple finite element simulations that were seeded with different wavelengths. In each of these models, I created a mesh that had a unique even surface harmonic, but kept the elastic, viscous, and plastic properties the same. In all tested cases however, there were no conditions in which observable folding could be induced. It was only when the strains approached ~10%, which is an order of magnitude greater than the inferred amount, that it became possible to induce folding that could explain the observed topography.

D. Simulating Spatial Variations of Lithospheric Folding in the South Polar Terrain of Enceladus

Given my findings that 1) Folding occurs on global scales with large strain, but not on regional scales with low strain, I was curious whether it was possible to induce folding on a much smaller scale of feature, but still incorporate large strain (~10% or greater). The images that NASA's Cassini spacecraft has taken of Saturn's moon Enceladus show a tectonically active satellite with plumes emanating out of the south polar region. The geologic activity is concentrated in what has been called the South Polar Terrain (SPT), which consists of young, tectonically disrupted terrain that is separated from the rest of Enceladus by a distinct boundary hundreds of meters high. Within this terrain, the region is further marked by prominent, long, parallel fractures known as "tiger stripes," high heat flow, and water ice plumes originating at the tiger stripes. In addition to the tiger stripes, the main landform found in the SPT is sub-parallel to parallel ridges and troughs. These include those that strike roughly parallel to the boundary at ~55° S latitude between the SPT and the rest of Enceladus, which have wavelength of ~5 km and amplitude of several hundred meters. High-resolution images of the south pole of Enceladus have also revealed regions of closely spaced quasi-linear features (dubbed "ropy" terrain) that exist between the tiger stripes and have wavelength of ~1.1 km. It has been hypothesized that the "ropy" terrain appeared similar to the ropy pahoehoe commonly found in Hawaii volcanoes, which formed under a compressional stress acting on the colder (more viscous) layer of the lava, causing folding. I thus created a suite of simulations of the two sets of Enceladus features using a high surface temperature, high heat flow, and a temperature-dependent viscosity profile. I found that the features form under a narrow but realistic range of starting conditions and that the longer the initial wavelength the more amplification that was possible. Primarily, my work suggests that the SPT region had small amplitudes of initial topography and underwent contraction to accommodate the formation of the tiger stripes. As the region underwent larger strain (approaching 50%), the ropy terrain developed at the approximate amplitude that is observed today. Similarly for the putative folds at the boundary of the SPT) form under a wider range of strains (20-70%) and that are dependent on the values for heat flow and surface that are used.

My dissertation makes significant contributions to the ways in which contractually induced folding can and cannot produce long-wavelength topography across three bodies within our solar system. These results suggest that only situations in which large strain is induced (strains larger than 10%) are capable of producing folding of the lithosphere, in agreement with other recent studies of unstable lithospheric deformation.

CHAPTER II

II. FORMATION OF THE BULGE OF IAPETUS THROUGH FOLDING

Chapter II will be submitted to Icarus as:

Jonathan P. Kay[1] and Andrew J. Dombard[1]

1 - The Department of Earth and Environmental Sciences (MC-186), University of Illinois at Chicago, 845 W. Taylor St., Chicago, IL 60607, USA.

A. Abstract

Previous models that attempted to explain the formation of the pronounced oblate shape of Iapetus suggested that it was a preserved rotational bulge. These models assumed that the heating was provided by short-lived radioactive isotopes that decayed rapidly and allowed the excess flattening of the lithosphere to be locked in by a thickening lithosphere, but placed severe timing constraints on the formation of Iapetus and its bulge. Here, we show that finite element simulations with an elastic-viscous-plastic rheology indicate it is possible to form the bulge through long-wavelength folding of the lithosphere of Iapetus during an epoch of contraction combined with a latitudinal surface temperature gradient. Heat generated by long-lived radioactive isotopes warms the interior causing a porosity loss and forces it to compact by ~10%. The simulations are most effective when there is a 30 K temperature difference between the pole and the equator. The bulge develops regardless of the time of deformation. In addition, long term simulations show that when no stress is applied the mechanical lithosphere is strong enough to support the bulge, and therefore no relaxation is observed.

B. Introduction

The distinctly oblate shape (and peerless equatorial ridge) on Saturn's moon Iapetus is unique in our solar system (Porco et al. 2004; Thomas et al. 2010) (Fig. 1). The shape of Iapetus is best fit by an oblate spheroid where the difference between equatorial radius and polar radius is 35.0 ± 3.7 km (Thomas et al. 2007; Castillo-Rogez et al. 2007), yielding an ~4.5% flattening of the moon. (For comparison, the Earth's flattening is ~0.5%, an order of magnitude less.) This flattening has generally been attributed to a frozen-in shape from an epoch with a more rapid rotation rate (e.g., Thomas et al. 2007; Castillo-Rogez et al. 2007), because the observed figure of Iapetus is consistent with a body in equilibrium with a spin period of ~16 hours. This is different from the current spin period of 79.33 days (Castillo-Rogez et al. 2007).

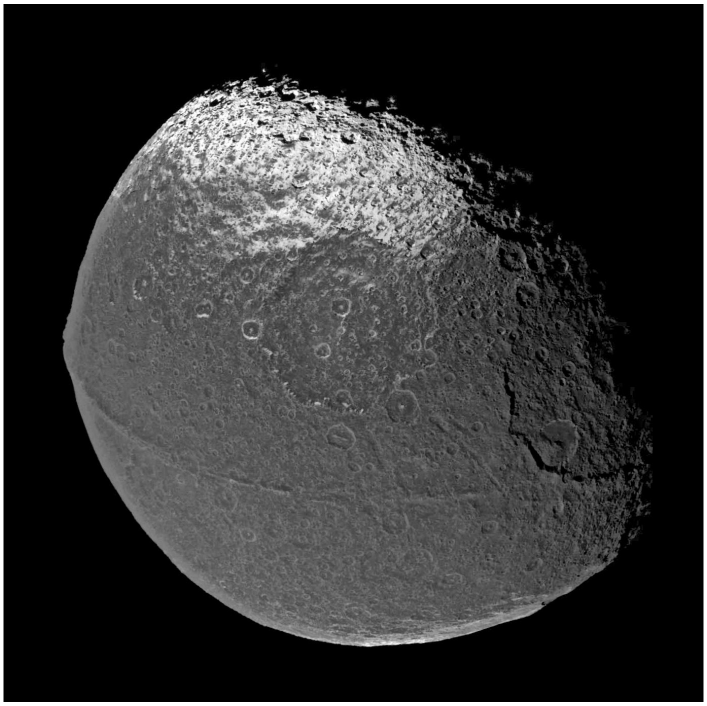

Figure 1: Saturn’s moon Iapetus, with its distinctly oblate spheroidal shape. (Courtesy NASA/JPL-Caltech PIA06166)

Researchers have sought to understand how the lithosphere of Iapetus could fossilize and preserve an ancient rotational bulge (Castillo-Rogez et al. 2007; Robuchon et al. 2010). These coupled thermal, orbital, and mechanical models showed that an initially porous satellite would need to have accreted within ~5 Myr of formation of the solar system. This is based on the available short-lived radioactive isotopes (SLRI) that are present in petrochemical models (Castillo-Rogez et al. 2007). This is the only situation in which there was tidal despinning of the satellite but a lithosphere sufficiently thick to freeze in the bulge after loss of rotational support. However, a satellite with the same high initial porosity, but with only long-lived radioactive isotopes (LLRI), while still slowing down rotationally, possessed a lithosphere too thin and weak to support the bulge. These results suggest that there are severe timing constraints on the formation Iapetus and the stabilization the surface.

These efforts, however, hinge on the assumption that the bulge is a remnant rotational structure. Could it instead have a tectonic origin, thereby bypassing these severe timing constraints that the SLRI place upon the formation of the bulge? As modeled by Castillo-Rogez et al. (2007) and Robuchon et al. (2010), heating by the LLRIs ^{40}K, ^{232}Th, ^{235}U, and ^{238}U would have warmed the interior of Iapetus and led to the loss of initial porosity, which in turn would have driven the entire icy lithosphere to deform to account for the loss of volume. Previous work by Sandwell and Schubert (2010) applied a buckling (elastic deformation) model of a uniform elastic shell and found that for shell thicknesses larger than 120 km, the preferred wavelength of buckling is at spherical harmonic degree 2, a buckling mode consistent with an oblate spheroid. Thus, axisymmetric degree-2 buckling could explain the currently observed flattening. The problem with the proposed elastic buckling model is that stresses required to buckle the lithosphere are far greater than the strength of the lithosphere -- ~280 MPa vs. ~12 MPa

(Sandwell and Schubert 2010). This stress paradox is a common shortcoming of elastic buckling models (e.g., Turcotte and Schubert 2014).

In this paper, we propose an alternative hypothesis that by simulating a variation in lithospheric thickness due to a pole-to-equator surface temperature during an epoch of planetary contraction while invoking a more realistic rheology (elastic-viscous-plastic vs. elastic), it is possible to reproduce tectonically the observed shape of Iapetus. This alternative formation mechanism of the bulge might make it possible to remove the severe time constraints that the rotational bulge models require.

C. Methods

We simulate the unstable deformation of a lithosphere, using an approach applicable for both long- and short-wavelength situations. For this project, we use the Marc finite element package (http://www.mscsoftware.com). Marc has been well-vetted in the study of the thermal and mechanical properties of the lithospheres of icy satellites and rocky planets (e.g., Dombard and McKinnon 2000; Dombard and McKinnon 2001; Dombard and McKinnon 2006a, b; Dombard et al. 2007; Dombard and Cheng, 2008; Damptz and Dombard 2011; Karimi et al. 2016). The code employs our composite rheology that describes the general behavior of geologic materials: elastic on short time scales and viscous on long time scales, with brittle failure (continuum plasticity) for high enough stresses.

Thus, we use a rheological model more consistent with observed deformational behavior of geologic materials, utilizing constitutive relations for elastic, viscous, and plastic (e.g., Gammon et al. 1983; Beeman et al. 1988; Goldsby and Kohlsedt 2001) behavior linked in series (a Maxwell viscoelastic solid extended to include a plastic component). For this type of composite rheology, the mechanical behavior can be explored with a Yield Strength Envelope (YSE), which is defined as the strength of the material under planetary conditions (i.e., temperature and pressure increasing with depth) and subjected to uniform, planar, horizontal contraction (or extension) at a constant rate (Fig. 2).

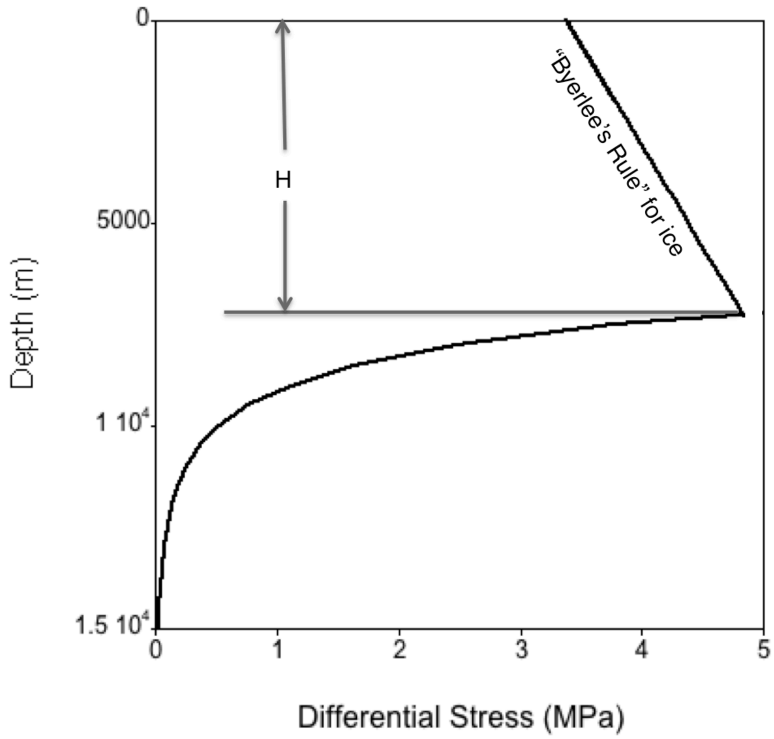

Figure 2: Example compressional yield envelop for Iapetus' lithosphere. The intersection occurs at the frictional and ductile yield strengths are equal for a constant strain rate and determines the thickness of the lithosphere (*H*), which is then assumed to have constant strength.

Two primary regimes are seen: 1) a shallow zone where strength is controlled by the brittle, frictional strength of the material (modeled here as continuum plasticity) and 2) a deeper zone in which ductile creep limits the strength, with the Brittle Ductile Transition (BDT) separating the two (e.g., Dombard and McKinnon 2006a, b, and references therein). Within the envelope, deformation is accommodated elastically. The brittle regime is assumed to have a strength that increases linearly with depth (i.e., pressure), a "Byerlee's rule" for cold ice (Beeman et al. 1998). This region is defined by a frictional slip criterion with finite cohesion and is largely independent of temperature and strain rate. For low confining stresses, experimental data have shown two relationships, one with finite cohesion and one with zero cohesion:

$$\tau = 0.55\sigma_n + 1.0MPa \qquad (1)$$

$$\tau = 0.69\sigma_n \qquad (2)$$

where, τ is the shear stress required for slip and σ_n is the normal stress (Beeman et al. 1998). While these shear failure criteria are both consistent with the experimental data, we use Eq. 1 to preclude strengthless material in our numerical approach.

Below the BDT, viscous creep dominates and is sensitive to temperature and, to a lesser degree, to strain rate (Durham and Stern 2001; Goldsby and Kohlstedt 2001). Consequently, the depth to the BDT, and hence the lithospheric thickness, primarily depends on thermal state. The ductile flow of ice occurs by multiple mechanisms operating simultaneously. There are three different dislocation creep mechanisms, one of which dominates over the other two in differing temperature bands (Durham and Stern 2001). Dislocation creep occurs by movement of imperfections (dislocations) through the crystal lattice of materials. In addition, there are two other creep regimes that act in a rate limiting sense, dislocation in an Easy-Slip (ES) system and a grain-size sensitive grain-boundary sliding (GBS) (Goldsby and Kohlstedt 2001). Finally, diffusion creep is expected to dominate under very low stress conditions (Goldsby and Kohlstedt 2001). Strain rates from dislocation creep add in series (i.e., the fastest one dominates the flow), as does diffusion creep, while ES and GBS act in parallel,

$$\dot{\varepsilon}_{visco} = \dot{\varepsilon}_a + \dot{\varepsilon}_b + \dot{\varepsilon}_c + \dot{\varepsilon}_{dif} + \left(\frac{1}{\dot{\varepsilon}_{ES}} + \frac{1}{\dot{\varepsilon}_{GBS}}\right)^{-1} \tag{3}$$

where *a, b*, and *c* denoted the three dislocation creep regimes and $\dot{\varepsilon}_{visco}$ represents the total equivalent strain rate. Each of these different creep regimes is a function of stress, temperature, and grain size (for GBS and diffusion creep) and take the form

$$\dot{\varepsilon}_E = A\left(\frac{1}{d}\right)^m \sigma_E^{In} e^{\left(\frac{-Q}{RT}\right)} \tag{4}$$

where $\dot{\varepsilon}_E$is the equivalent strain rate, σ_E^I is the equivalent deviatoric stress, *A* is a material dependent constant normalized for uniaxial deformation (e.g., Ranalli 1995), *d* is the grain size (assumed to be 1 mm), *n* is the power law exponent, *m* is the grain-size exponent, *Q* is the activation energy, *R* is the universal gas constant, and *T* is absolute temperature. For all creep regimes other than GBS and diffusion creep, *m*=0.

For Iapetus, we follow Sandwell and Schubert (2010) and consider a thermal model of a porous Iapetus with only LLRI (Castillo-Rogez et al. 2007; Robuchon et al. 2010). During an epoch of porosity loss that lasts of order 100 Myr, ~10% horizontal shortening of the lithosphere can occur with a surface heat flux of order 1 mW m^{-2}. As has been done previously for icy bodies (e.g., Dombard and McKinnon, 2000; Dombard and McKinnon, 2001; Dombard and McKinnon, 2006a, 2006b; Dombard et al., 2007; Dombard and Cheng, 2008; Damptz and Dombard, 2011; Bland et al., 2012), we employ the thermal and mechanical material parameters for water ice I_h (Gammon et al., 1983; Beeman et al. 1988; Durham and Stern 2001; Goldsby and Kohlstedt 2000). Water ice exhibits a temperature-dependent thermal conductivity given by $651/T$, where T is temperature (Petrenko, and Whitworth, 1999).

Fig. 3 shows the role of thermal conductivity on the temperature profile. A critical component of the thermomechanical models (Castillo-Rogez et al. 2007; Robuchon et al. 2010) and their application here is that the interior and near surface are porous. Porosity has the effect of decreasing the thermal conductivity by restricting the pathways through which heat can diffuse. Consequently, we consider conductivities that are 1/3 and 1/2 that of intact ice. Fig. 3a shows that for a heat flow of 0.75 mW m^{-2}, the thermal conductivity with must be lower than that of intact ice in order for the interior to get warm enough to initiate porosity loss (120 K), which drives the planetary contraction (Castillo-Rogez et al. 2007). This concept is further explored in Fig. 3b, where a range of heat flows are explored for a conductivity half that of intact ice.

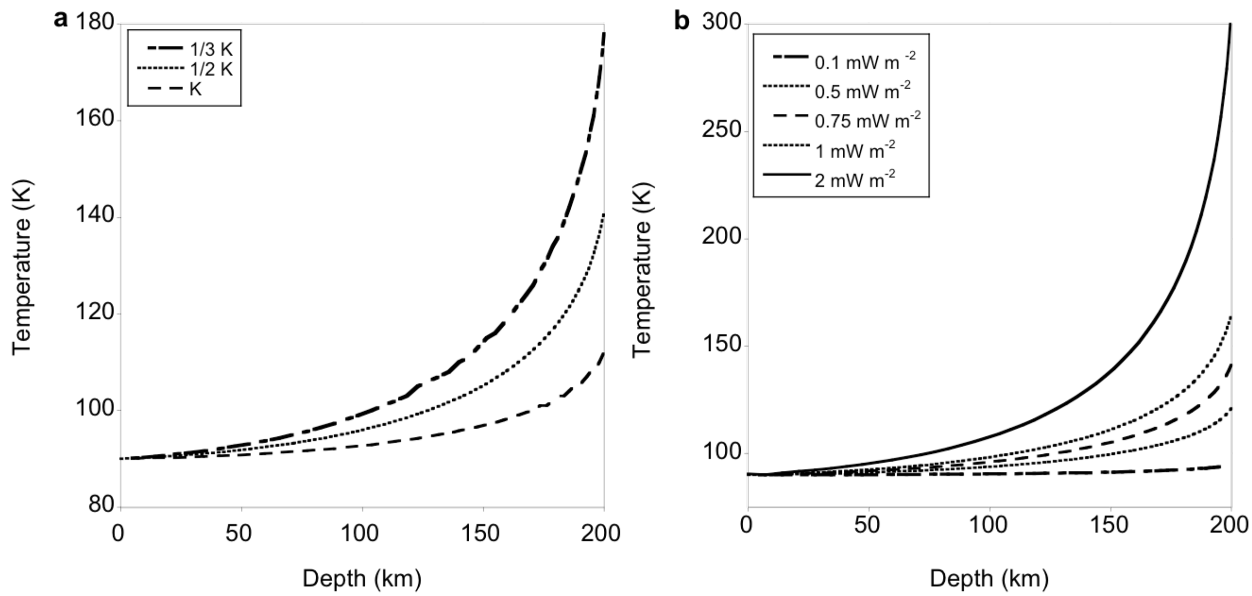

Figure 3: (a) Temperature depth profile for three different thermal conductivities of $217/T$, $325/T$, and $651/T$ with a heat flow of 0.75 mW m^{-2}. (b) The relationship between heat flow and temperature for a conductivity of $325/T$.

For our finite-element domain, we take advantage of symmetry across the equator and axisymmetry around the spin pole to model a slice through one hemisphere. We assume a pre-contraction radius of 800 km, ~10% larger than the current mean radius of Iapetus (735 km). Application of a volume change in the deep interior in order to drive the lithospheric shortening is a technical challenge; however, details of the deformation in the deep interior is less of a concern here. To simplify the boundary conditions, particularly the imposition of the lateral shortening, we unwrap the spherical hemisphere into a planar configuration (a cylinder), with the equator on the outer edge and the pole at the axisymmetric center; in this geometry, the effect of volume change in the interior on the lithosphere can be modeled as a forced, uniform displacement on this outside edge (Fig. 4a). A corollary is that the simulations thus will not include membrane support that arises on a curved spherical surface, a choice this is not anticipated to affect the results, but will be discussed later. At the heat flows to be simulated here, ductile creep effectively renders the material below ~200 km as possessing negligible strength and should thus have little effect on the simulations. As a result, our meshes have a depth of 200 km. Simulations were run with deeper meshes confirmed this. This domain has been subdivided into 5000 finite elements (50 in depth and 100 in width). A slight bias was applied toward the surface of the mesh to concentrate elements where the deformation of interest is occurring. In addition, we also consider meshes that had finer resolution in order to test the sensitivity of our modeling to the folding, finding they were largely invariant of mesh resolution.

We first perform a series of steady-state thermal simulations to determine the temperature field, and the results of the thermal simulations are piped into the corresponding mechanical simulations. For our initial thermal simulations, we solve for the steady state equilibrium between a fixed surface temperature and a constant applied basal heat flux (and assume zero heat flux on the mesh sides). We consider a range of basal heat fluxes of 0.1-5 mW m^{-2}, which brackets the expected heat flow out of Iapetus during this epoch (Castillo-Rogez et al. 2007; Robuchon et al. 2010). In these types of simulations of unstable lithospheric deformation, the domain will uniformly thicken unless there is something to break horizontal uniformity. Here, this perturbation will be applied with a variable surface temperature, because of our hypothesis that latitudinal variations in the thickness of the lithosphere control the deformation. Surface temperatures is set to follow a fourth-root of the cosine of latitude, and range from around 60 K at the pole to around 90 K at the equator (Spencer and Denk, 2009).

For the mechanical simulations, a gravitational load controls the brittle strength envelope and produces surface buoyancy forces that restrict vertical deformation. We assume a density of 950 kg $m^{-3}$and a gravity of 0.22 m s^{-2}. The applied boundary conditions allow for a free slip surface on both the bottom and on the sides. Additionally, the outside edge will be forced in by 115 km linearly over our simulated time of ostensibly 100 Myr (other timespans have been tested). Furthermore, additional simulations with a fixed outside boundary are performed to explore the relaxation of the bulge after the epoch of contraction has ended (Fig. 4b).

The time steps used in the simulations are governed by the minimum Maxwell time in the mesh, which is dependent upon the elastic moduli and viscosity (e.g., Turcotte and Schubert, 2014). A higher temperature leads to lower viscosities, and therefore to smaller Maxwell times and smaller time steps. In order to keep the running time for simulations tractable (days to weeks), we limit the minimum viscosity in the mesh to 10^{21} Pa s. We have tested this viscosity cut-off with smaller minimum viscosities (e.g., 10^{20} Pa s), which led to longer run times but similar results.

For these simulations, we implement a full large strain formulation, which includes the second-order term of the strain displacement relationship and a geometric update. During the simulation, the mesh geometry changes continuously, and since topography is a source of stress, updating the geometry is required. Additionally, we apply a constant dilatation scheme that controls numerical errors that yield over-stiff elements while simulating nearly incompressible behavior (e.g., viscous creep). The gravity causes the material in the mesh to compact slightly. To counter this self-compaction, the mesh is seeded with an initial stress that is equivalent to the overburden stress. We define a successful simulation as one that yields a differential surface displacement greater than the observed radial difference of 35 km (greater than in order to account for any post-formation relaxation of the bulge).

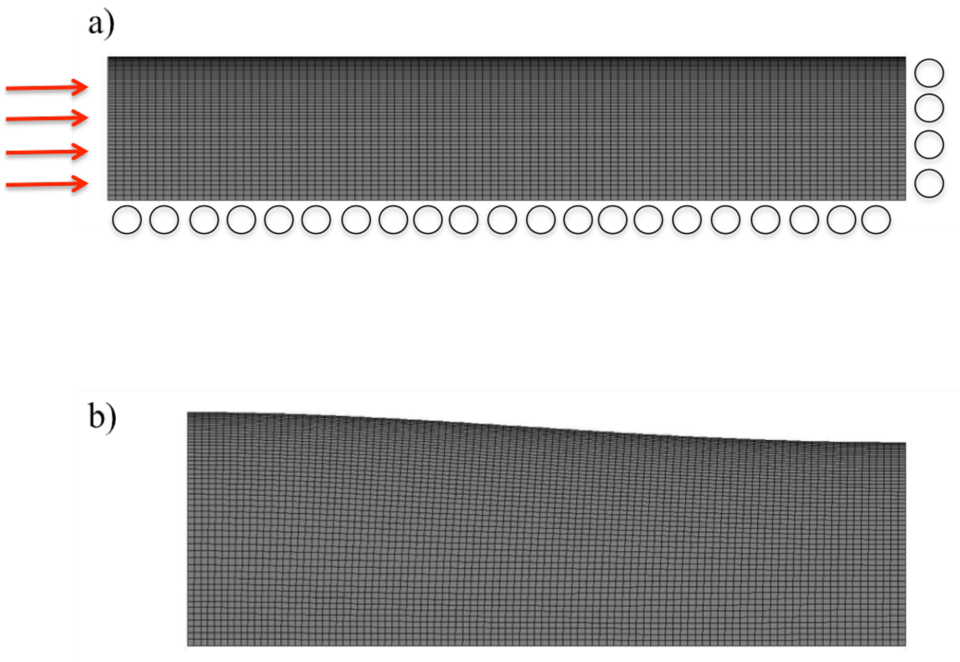

Figure 4: a) The undeformed mesh has a width of 1,115 km (i.e., 1/4 the circumference of Iapetus), a depth 200 km, and has the axis of axisymmetry on the right. There is a slight element biasing toward to the surface to improve resolution in the deforming lithosphere. The red arrows represent the direction of contraction and the rollers represent a free slip surface. b) This is our best-case model, which produces 45 km of deformation.

D. Results

We have explored a broad range of conditions for the formation of the bulge via folding. We first describe the model in which the geometry of the final mesh best matches the observed deformation. The best-case model is shown in Fig. 5 and Fig. 6. The simulation uses a heat flux of 0.5 mW m^{-2}, an effective surface temperature range of 60 K at the pole and 90 K at the equator, and a thermal conductivity of one-half that of intact ice. All other parameters are as described above. The planar simulations demonstrate the development of an equatorial bulge when the surface temperature varies with latitude. Because of a thinner lithosphere at low latitudes, the deformation is concentrated at low latitudes, preferentially lifting the surface relative to high latitudes. The transition in surface uplift is smoothly varying, following the transition in surface temperature (and hence lithospheric thickness); however, the deformation is skewed ~10-20° equator-ward away from a cosine shape (Kay and Dombard 2011).

In the first 100 kyr of our simulation, we see only 20 m of difference between the equatorial and polar radii. After 1 Myr, only a few 100 m of difference has developed. It is not until 75 Myr that we see the currently observed amount of deformation, ~40 km. At this point, the yield strength envelope becomes saturated and additional shortening is accommodated through continued unstable deformation. At 100 Myr, the difference is ~45 km, in excess of the observed difference. These simulations suggest that this is a plausible mechanism for the oblate shape of Iapetus.

These first results (Fig. 5a) show simulations that are capable of producing the largest difference between equatorial and polar radii, which included a thermal conductivity of $325/T$ and a heat flow of 0.5 mW m^{-2}. Three different latitudinal surface temperature differences are shown: 50 to 80 K, 60 to 90 K, and 70 to 100 K. The simulations with the current surface temperature difference of 60 to 90 K yield the most differential displacement, producing ~45 km of radial difference. Simulations with a temperature difference of 70 to 100 K produced slightly less deformation of approximately 40 km. While the simulations with a temperature difference of 50 to 80 K produces a surprising 6 km of difference, suggesting the lithosphere is too cool and stiff to deform in this manner.

Additional results shown in Fig. 5b detail simulations under similar conditions as in Fig. 4a, but with a heat flow of 0.75 mW m^{-2} (a heat flow 50% larger). The simulations with a surface temperature difference of 60 to 90 K produced over 37 km of difference, still large but less than for the lower heat flow, which suggests the thinner lithosphere is less able to grow and support an oblate shape for the moon. Simulations with a temperature difference of 70 to 100 K produced slightly less deformation of ~34 km, consistent with Fig. 4a. In contrast to Fig. 5a, however, the simulations with a temperature difference of 50 to 80 produces a surprising 42 km of difference, again somewhat larger than what is observed. Here, the higher heat flow compensates for the stiffening effect on the lithosphere of the lower surface temperature range.

Fig. 5c shows the influence that thermal conductivity has on our simulations. These simulations assume a 60-90 K surface temperature differential. Plotted are three different thermal conductivity values with a heat flow of 0.75 mW m^{-2}: 651/*T* (i.e., that of intact ice), 325.5/*T*, and 217/*T*. Each of these simulations are capable of producing deformation greater than 30 km, with 651/*T* producing 31 km, 325.5/*T* producing 37 km, and 217/*T* producing 30.4 km.

Fig. 5d builds on Fig. 4a by showing several different heat flow values centered on our optimal heat flow result: 0.5, 0.75, 1.0, and 2.0 mW m^{-2}, , The deformation is largest at 0.5 mW m^{-2} and decreases as the heat flow increases and decreases. Not shown are results for heat flows of 0.1 mW $m^{-2,}$ and 5 mW m^{-2}, which produced negligible deformation.

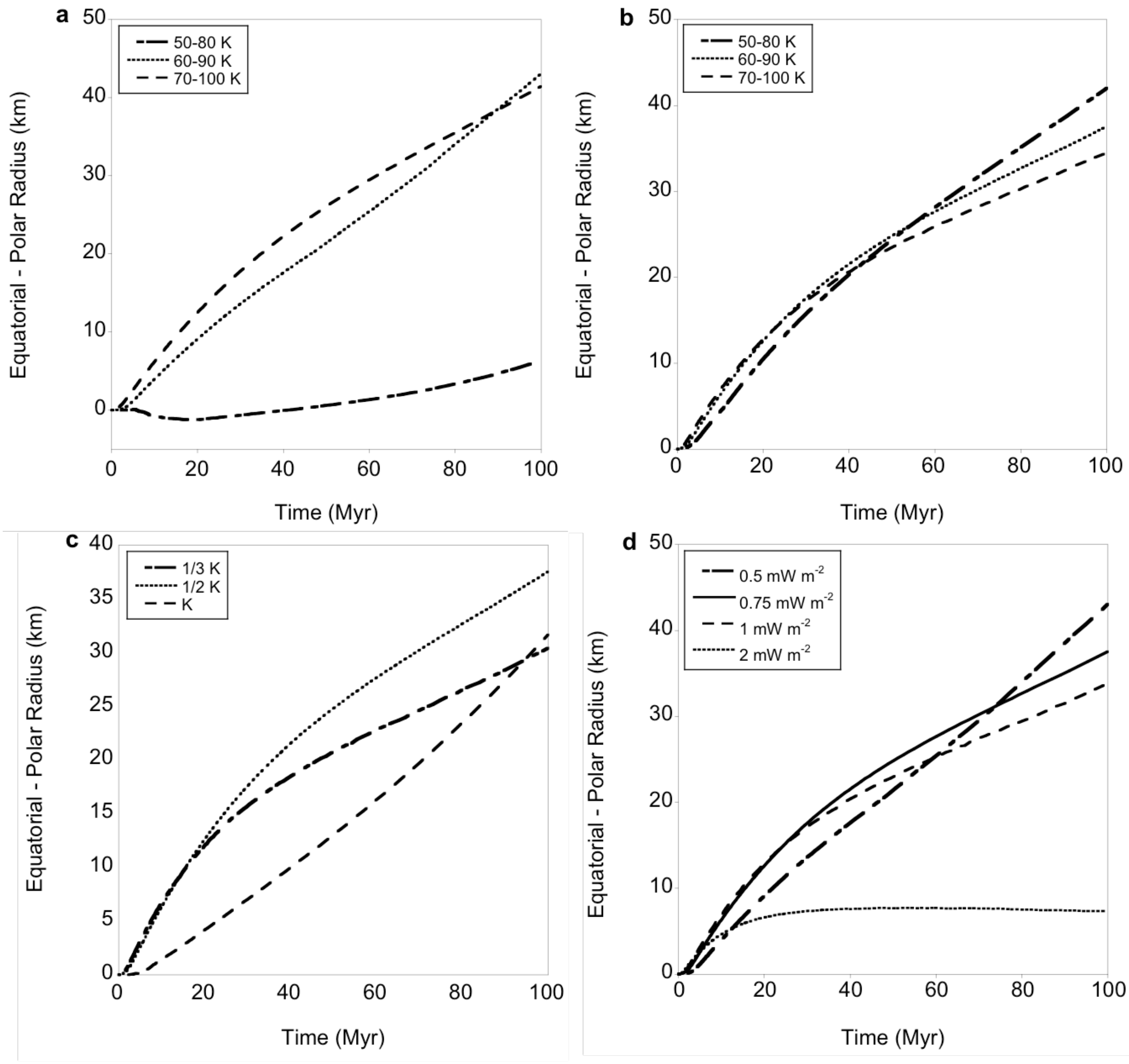

Figure 5: Plots of the difference in equatorial and polar radii as a function of time. (a) These simulations include a conductivity of $325/T$ and a heat flow of 0.5 mW m^{-2}. Three different latitudinal surface temperature differences are shown: 50 to 80 K, 60 to 90 K, and 70 to 100 K. (b) Same as (a), but with a higher heat flow of 0.75 mW m^{-2}. (c) This figure shows the influence that thermal conductivity has. Plotted are three different thermal conductivity values ($651/T$, $325.5/T$, and $217/T$) with a heat flow of 0.75 mW m^{-2} and a surface temperature range of 60 to 90 K. (d) This figure shows several different heat flow values centered around our optimal heat flow result (a). Shown are heat flow values of 0.5 mW m^{-2}, 0.75 mW m^{-2}, 1.0 mW m^{-2}, and 2.0 mW m^{-2}. with a conductivity of 325.5, the deformation is largest around 0.5 mW m^{-2}. Not shown are cases with heat flows of 0.1 mW m^{-2} and 5 mW m^{-2} that produced negligible deformation.

We have also attempted a series of simulation that include a topographicly pre-seeded rotational bulge, implemented as a half cosine higher at the equator than at the pole by a prescribed amount. We consider initial amplitudes of 5 and 1000 m (Fig. 6). Final results are comparable to the simulations without the pre-seed. Clearly, the addition of the pre-simulation topography did not have much influence on the growth rates of the bulge, and this effect is primarily a function of the latitudinally variable lithospheric thickness due to differences in surface temperature.

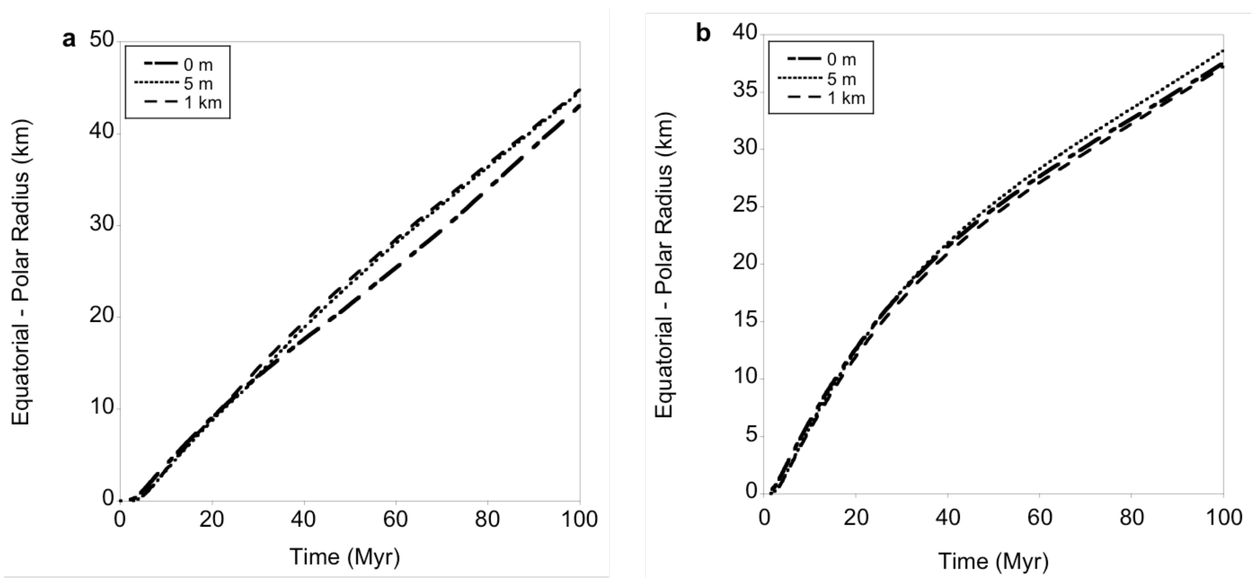

Figure 6: (a) Simulations for a 0, 5, 1000 m topographic pre-seed for a heat flow 0.5 mW m^{-2}. (b) Simulations for a 0, 5, 1000 m pre-seed for a heat flow of 0.75 mW m^{-2}.

We have also run a series of simulations that attempt to measure the relaxation of the bulge. For these, we stop the forced lateral displacements, and maintain free-slip conditions on both side boundaries. These simulations were run under our optimal conditions using a heat flow of 0.5 mW m^{-2}, a conductivity of ½ that of intact ice, and a surface temperature profile of 60-90. These simulations ran for 1 Gyr and do not show any appreciable change to the size of the bulge with an Equator – polar radius starting at 45 km and ending at 44.5 km. These results indicate that the conditions that permit the formation of the bulge via this tectonic process also allows the long term retention of this bulge.

To test consequences of a ice I with a high porosity we ran simulations with a lower density (~900 kg m^{-3}), a lower Young's Modulus (90 MPa and 900 MPa), and simulations with both of these parameters alerted. The lower density values increased the amount of deformation. This is potentially a result of the lower density ice being less resistant and easer to induce flow. No difference is developed for the Young's Modulus two orders of magnitude lower and only 300 m of difference is developed for a Young's Modulus of 900 MPa. Both of these results suggest that the ice at depth is largely intact due to the lack of isostatic support. This would be true for both the rotational bulge and the porosity collapse induced bulge.

E. Discussion

The results presented in the previous section show that it is possible to reproduce a bulge via folding under reasonable conditions, which include a heat flow between 0.5 and 1.25 mW m^{-2}, a thermal conductivity 50 to 75% that of intact ice, and a surface temperature difference between the pole and the equator of 30 K**.** With our simulations, we can produce ~45 km of radial difference, greater than the amount currently observed ~ 35 km. Additionally, it is conceivable that initial bulge was much larger and has subsequently relaxed over time (Dombard and Cheng 2008; Robuchon et al. 2010), and therefore any model that explains the bulge must be able to produce a larger bulge than is currently observed; however as discussed previously, our simulations that tested relaxation did not show any appreciable amount.

These simulations implicitly assume a differentiated Iapetus; however even if Iapetus is undifferentiated, the bulk density of the satellite is so low (~1200 kg m^{-3}) that Iapetus would be essentially a slightly dirty ice ball (e.g., Tyler et al., 1982). Experiments have indicated that a low volume fraction of hard particulates in ice only stiffen the ductile creep by a modest degree (Durham et al. 1997), so we therefore do not expect our conclusions to change much as compared to "clean" ice. Recent simulations that examined the mechanical properties of ice I–magnesium sulfate, essentially dirty ice, exhibit viscoelastic properties similar to that of water ice (Golding et al. 2013). Therefore, even if the outer regions of Iapetus is not made of pure water ice, the rheological properties will be comparable, and our results will hold.

There appears to be a small temperature range (but not unreasonably so) under which ideal conditions are established for growth of a bulge. The role of the conductivity of the ice is significant and will influence the thermal lithosphere and thus the thickness. These two parameters are interconnected and would be difficult to identify exact heat flows without understanding the porosity as a function of depth in the lithosphere. A heavily fractured lithosphere would increase the void space and could potentially decrease the thermal conductivity (Maston and Nash, 1983; Warren and Rasmussen, 1987), which in turn would increase the temperatures at depth.

There also exists the possibility that the surface temperature values were in the lower range (due to a dimmer sun), but that these values could be compensated by invoking ice that heavily fractured and a higher heat flow (due to presence of a larger concentration of LLRI's). The temperature profile applied to the surface is a best approximation of what we know about early Iapetus. The exact temperature profile will play a large role in the amount of deformation that is produced.

Under this thermal scenario, the lithosphere of Iapetus (defined by the brittle-ductile transition) is ~100 km thick, thereby likely forcing the folding to long wavelengths. Whether degree 2 (i.e., the wavelength scale associated with the oblate shape of Iapetus) is dominant is unclear, and indeed, Sandwell and Schubert (2010) argued that a large topographic seed in the form of a small rotational bulge might force the deformation to an oblate spheroidal shape. Our results, on the other hand, show that latitudinal variations in the strength of the lithosphere due to surface temperature change dominates over a topographic perturbation (Fig. 5). As a corollary, shorter folding instability wavelengths will get forced to degree-2 by the lithospheric thickness variability.

One aspect that is not included in our planar model is the membrane response of a spherical lithosphere, which would tend to resist the folding deformation that we observe. We can estimate the effect of this membrane resistance. As shown in Turcotte et al. (1981), membrane support starts to become appreciable when the horizontal scale of deformation is comparable to a spherical harmonic degree approximately given by the square root of the planetary radius divided by the lithospheric thickness. For our lithospheric thicknesses seen here (~100 km), this transitional spherical harmonic degree is ~2-3, meaning that membrane resistance is only just becoming a factor at the scale in question. By over-predicting the amount of radial difference (up to ~45 km), our planar simulations can compensate for the missing membrane response. Conversely, the addition of a membrane effect would also retard long-term relaxation of the bulge. Taken together, our conclusions will likely hold despite our planar geometry.

F. Conclusions

The shape of Iapetus is well fit by an oblate spheroid for which the difference between equatorial radius and polar radius is ~35 km. The bulge has previously been attributed to a frozen-in shape from an epoch with a more rapid rotation rate, because the observed figure of Iapetus is consistent with a body in equilibrium with a spin period of ~16 hours, compared to the known current spin period of 79.33 days. We use the finite element method with an elastic-viscous-plastic rheological model to simulate the long-term global scale folding of Iapetus to determine it is possible to form tectonically the equatorial bulge for a reasonable, but narrow, band of heat flux (0.5-1.25 mW m^{-2}), thermal conductivity (50 to 75% that of normal ice), and surface temperature difference between the pole and the equator of 30 K. Additionally, long-term simulations show that this equatorial bulge would not then subsequently relax over billion year time scales. These results indicate that the distinctly oblate shape of Iapetus does not need to be a relic rotational bulge, which alleviates the severe timing constrains on the formation of Iapetus and its bulge indicated by past models (e.g., Castillo-Rogez et al. 2007; Robuchon et al. 2010).

G. References:

Bland, M.T., Ross A.B., and Adam P.S., 2007. "Unstable Extension of Enceladus' Lithosphere." *Icarus* 192 (1) (December 1): 92–105. doi:10.1016/j.icarus.2007.06.011.

Bland, M. T., McKinnon, W. B., 2012. Forming Europa's folds: Strain requirements for production of large-amplitude deformation, *Icarus* 221, 694-709.

Canup, R. M., 2004. Simulations of a late lunar-forming impact. *Icarus*. 168, 433-456.

Castillo-Rogez, J. C., Matson, D. L., Sotin, C., Johnson, T. V., Lunine, J. I., and Thomas, P. C., 2007. Iapetus' geophysics: Rotation rate, shape, and equatorial ridge. Icarus. 190, 179-202.

Czechowski, L. and Leliwa-Kopystyn´ski, J., 2008. The Iapetus's ridge: Possible explanations of its origin. Advances in Space Research. 42, 61-69.

Dombard, A.J., McKinnon, W.B., 2000. Long-term retention of impact crater topography on Ganymede. J. Geophys. Res. 27 (22), 3663–3666.

Dombard, A.J., McKinnon, W.B., 2001. Formation of grooved terrain on Ganymede: extensional instability mediated by cold, superplastic creep. Icarus 154, 321-336.

Dombard, A.J., McKinnon, W.B., 2006a. Elastoviscoplastic relaxation of impact crater topography with application to Ganymede and Callisto. J. Geophys. Res. 111, E01001. doi:10.1029/2005JE002445.

Dombard, A.J., McKinnon, W.B., 2006b. Folding of Europa's icy lithosphere: An analysis of viscous-plastic buckling and subsequent topographic relaxation. J. Struct. Geol. 28, 2259–2269.

Dombard, A.J., Patterson, G.W., Prockter, L.M., 2007. Sill injection on icy satellites inferred from ridge-induced flexure on Europa. EOS Trans. AGU (Fall Meet. Suppl.) 88(52).

Dombard, A. J. and Cheng, A. F., 2008. Constraints on the Evolution of Iapetus from Simulations of Its Ridge and Bulge. Lunar Planet. Sci. XXXIX, 2262.

Dombard, A. J., Cheng, A. F., McKinnon, W. B., and Kay J.P. 2010. The Weirdest Topography in the Outer Solar System: The Ridge on Iapetus and its Possible Formation via Giant Impact. AGU Fall Meeting Abstracts. P31D-01.

Damptz, A.L., Dombard, A.J., 2011. Time-dependent flexure of the lithospheres on the icy satellites of Jupiter and Saturn. Icarus 216, 86-88.

Durham, W. B., and L. A. Stern 2001. Rheological properties of water ice— Applications to satellites of the outer planets. *Annu. Rev. Earth Planet. Sci.* **29**, 295–330.

Giese, B., Denk, T., Neukum, G., Roatsch, T., Helfenstein, P., Thomas, P. C., Turtle, E. P., McEwen, A., and Porco, C. C., 2008. The topography of Iapetus' leading side. Icarus. 193, 359-371.

Goldsby, D. L., and D. L. Kohlstedt 2001. Superplastic deformation of ice: Experimental observations. *J. Geophys. Res.* **106**, 11,017–11,030.

Golding, N, Burks, C.E., Lucas, K.N., Fortt, A.F., Snyder, S.A., and Schulson, E.M., 2013. Mechanical Properties of the Ice I–magnesium Sulfate Eutectic: A Comparison with Freshwater Ice in Reference to Europa. Icarus 225 (1): 248–256. doi:10.1016/j.icarus.2013.02.037.

Fink, J.H., Fletcher, R.C., 1981. In: Variations in Thickness of Ganymede's Lithosphere Determined by Spacings of Lineations. Abstracts of the Lunar and Planetary Conference XII, pp. 277e278.

Ip, W.-H., 2006. On a ring origin of the equatorial ridge of Iapetus. Geophys. Res. Lett.. 33, 16203.

Jacobson, R. A., P. G. Antreasian, J. J. Bordi, K. E. Criddle, R. Ionasescu, J. B. Jones, R. A. Mackenzie, M. C. Meek, D. Parcher, F. J. Pelletier, W. M. Owen Jr., D. C. Roth, I. M. Roundhill, and J. R. Stauch, 2006. The Gravity Field of the Saturnian System from Satellite Observations and Spacecraft Tracking Data. AJ. 132, 2520-2526.

Kay, J.P., Dombard, A.J., 2011. Unstable deformation and the formation of the equatorial bulge of Iapetus. Lunar Planet. Sci. XLII. Abstract 2441.

Kieffer, S. W., X. Lu, C. M. Bethke, J. R. Spencer, S. Marshak, and A. Navrotsky 2006, A clathrate reservoir hypothesis for Enceladus' south polar plume, Science, 314(5806), 1764–1766, doi:10.1126/ science.1133519.

Kokubo, E., Ida, S., and Makino, J., 2000. Evolution of a Circumterrestrial Disk and Formation of a Single Moon. Icarus. 148, 419-436.

Langseth, M.G., Keihm, S.J., Peters, K., 1976. Revised lunar heat-flow values. Proc. Lunar Planet. Sci. Conf. 7th, pp. 3143–3171

Matson, D.L., Nash D.B., 1983. Io's atmosphere – Pressure control by regolith cold trapping and surface venting J. Geophys. Res., 88, pp. 4771–4783

Melosh, H. J., 1977. Global tectonics of a despun planet. Icarus. 31, 221-243.

Petrenko, V.F., Whitworth, R.W., 1999. Physics of Ice. OUP Oxford.

Porco, C. C., et al., 2005. Cassini Imaging Science: Initial Results on Phoebe and Iapetus. Science. 307, 1237-1242.

Porco, C.C., Helfenstein, P., Thomas, P.C., Ingersoll, A.P., Wisdom, J., West, R., Neukum, G., Denk, T., Wagner, R., Roatsch, T., Kieffer, S., Turtle, E., McEwen, A., Johnson, T.V., Rathbun, J., Veverka, J., Wilson, D., Perry, J., Spitale, J., Brahic, A., Burns, J.A., DelGenio, A.D., Dones, L., Murray, C.D., Squyres, S., 2006. Cassini Observes the Active South Pole of Enceladus. Science 311, 1393–1401.

Ranalli, 1995 G. Ranalli Rheology of the Earth. Springer Science & Business Media (1995)

Roberts, J. H. and Nimmo, F., 2009. Tidal Dissipation Due to Despinning and the Equatorial Ridge on Iapetus. Lunar Planet. Sci. 40, 1927.

Robuchon, G., Choblet, G., Tobie, G., Cadek, O., Sotin, C., Grasset, O., 2010. Coupling of thermal evolution and despinning of early Iapetus, Icarus, 207, 959-971.

Sandwell, D. and G. Schubert, 2010. A contraction model for the flattening and equatorial ridge of Iapetus. Icarus. 210, 817-822.

Spencer, J.R., Barr, A.C., Esposito, L.W., Helfenstein, P., Ingersoll, A.P., Jaumann, R., McKay, C.P., Nimmo, F., Waite, J.H., 2009a. Enceladus: An active cryovolcanic satellite. In: Saturn after Cassini–Huygens. Springer, New York, pp. 683–722.

Spencer, J. R. and T. Denk, 2010. Formation of Iapetus' Extreme Albedo Dichotomy by Exogenically Triggered Thermal Ice Migration. Science. 327, 432.

Stewart, S. T. and Z. M. Leinhardt, 2009. Velocity-Dependent Catastrophic Disruption Criteria for Planetesimals. ApJ. 691, L133-L137.

Thomas, P. C., et al., 2007. Shapes of the saturnian icy satellites and their significance. Icarus. 190, 573-584.

Tyler, G.L., Eshleman, V.R., Anderson, J.D., Levy, G.S., Lindal, G.F., Wood, G.E., Croft, T.A., 1982. Radio science with Voyager 2 at Saturn - Atmosphere and ionosphere and the masses of Mimas, Tethys, and Iapetus. Science 215, 553–558. doi:10.1126/science.215.4532.553

Turcotte, D. L., R. J. Willemann, W. F. Haxby, J. Norberry, Role of membrane stresses in support of planetary topography, *J. Geophys. Res.*, 86, 3951–3959, 1981.

Turcotte D.L., Schubert, G., 2014 Schubert Geodynamics Cambridge University Press 3rd edition.

Warren, P.H. and K.L. Rasmussen., 1987. Megaregolith insulation, internal temperatures, and bulk uranium content of the Moon J. Geophys. Res., 92, pp. 3453–3465

CHAPTER III

III. A TEST FOR DEVELOPING LONG-WAVELENGTH LITHOSPHERIC FOLDING ON MERCURY

Chapter III will be submitted to Icarus as:

Jonathan P. Kay[1] and Andrew J. Dombard[1]

1 - The Department of Earth and Environmental Sciences (MC-186), University of Illinois at Chicago, 845 W. Taylor St., Chicago, IL 60607, USA.

A. Abstract:

Previous work has identified several regions where Mercury appears to have long-wavelength topography. As part of this work lithospheric folding was invoked as a method of this accommodation that resulted from the contraction of Mercury due to cooling. We report here on finite element simulations that have been designed to test the ability of the formation of long-wavelength topography via lithospheric folding within and near the Caloris Basin based on the strain generated from global cooling, which has been previously estimated to be as much as 10 km. We have modeled the formation of long-wavelength folds that are thought to have formed from contractionally induced instabilities after 3.8 Ga. Under expected surface temperatures of ~440 K, the simulations preserve the initial topography, but the development of even modest amplification in such low strain environments is untenable. In order to produce amplification of the lithosphere within range of what is presently observed, significantly higher (i.e., unrealistic) amounts of strain are required. Therefore, lithospheric folding cannot produce the observed long-wavelength topography on Mercury.

B. Introduction:

Models of the surface strain history of Mercury must be compatible with its thermal evolution (Solomon, 1976; Dombard et al., 2001; Hauck et al., 2004; Dombard and Hauck, 2008), which suggested pervasive and ongoing planetary contraction. There is ample evidence that Mercury has contracted since the Late Heavy Bombardment (LHB), which includes lobate scarps, wrinkle ridges, and high-relief ridges (Hauck et al., 2004; Melosh and McKinnon, 1988; Strom et al., 1975; Watters et al., 1998, 2004, 2009). The lobate scarps are believed to be asymmetric hanging wall anticlines atop a thrust fault (Strom et al., 1975; Watters et al., 2004) and are larger than wrinkle ridges. Wrinkle ridges are a low relief feature that is an anticlinal fold that also sits above a blind thrust fault (Smith et al., 2012). These two features have preserved the contraction that Mercury has undergone since the LHB and have been used to estimate a decrease in planetary radius of 1-7 km (Strom et al., 1975; Watters et al., 2004, 2009; Byrne et al., 2014).

Another subtler consequence of global contraction may have been the formation of long-wavelength, low-amplitude topography. This type of topography has been predicted to exist on Mercury, which may have formed as a result of folding of the lithosphere (Dombard et al., 2001; Hauck et al., 2004); however, it was not until the MESSENGER spacecraft began acquiring data of Mercury that the existence of long-wavelength topography was identified (Solomon, 1976; Smith et al., 2012). For example, altimetry and gravity data acquired in the Caloris impact basin (~60°N/115°E) showed that the smooth plains interior to the Caloris impact basin display long-wavelength variations in topography incongruous with an impact basin (Fig. 1) (Smith et al., 2012; Zuber et al., 2012). Portions of the northern floor of the basin lie higher in elevation than the basin rim, with variations in topography that can reach as high as 3 km (Smith et al., 2012;

Zuber et al., 2012). The northern portion of the Caloris floor has been observed to be part of a quasi-linear rise that trends west-southwest–east-northeast and extends over half of the circumference of Mercury, and only occurs at mid-latitudes (Solomon et al., 2012). The wavelength of the observed features has been estimated to be nearly 1000 km with an amplitude of ~3 km (Balcerski et al., 2012; Klimczak et al., 2013a). Balcerski et al. (2012) also observed that the tilts of superimposed, volcanically flooded impact craters were consistent with the modification of Mercury's long-wavelength topography that postdates both the volcanic plains emplacement and the pre-LHB formation of the Caloris basin (Head et al., 2008; Balcerski et al., 2012).

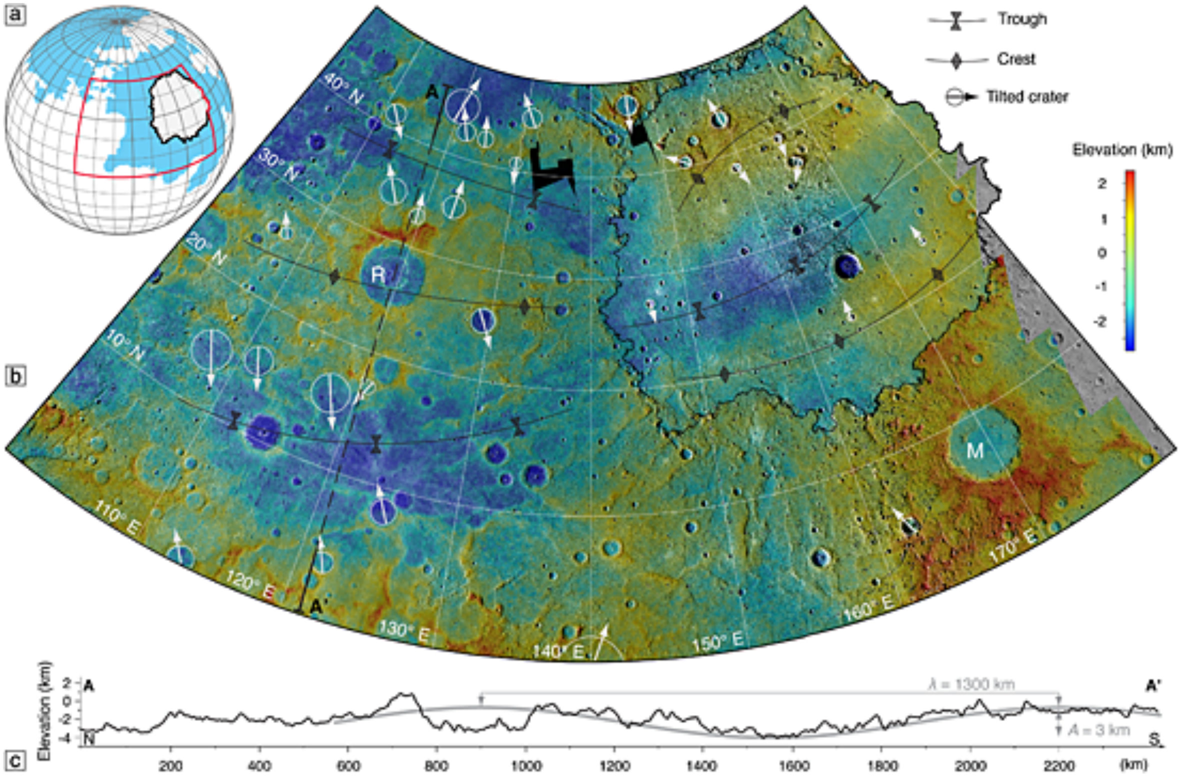

Figure 1: Map of the topography of the Caloris basin and surrounding smooth plains of Mercury that show volcanically flooded impact craters with floors that tilt away from the locus of highest elevation (adapted from Klimczak et al., 2013).

Is this long-wavelength topography evidence of the predicted folding of the lithosphere? Here, we test this idea using a finite element approach than employs a more realistic elastic-viscous-plastic rheological model than the semi-analytic viscous-plastic model that was used in the previous assessment (Dombard et al., 2001).

C. Methodology:

For this work, we use the commercially available MSC.Marc finite-element package, which has been well vetted in the study of lithospheres of icy satellites and rocky bodies (e.g., Dombard and McKinnon, 2006a, 2006b; Karimi et al., 2016; Karimi and Dombard, 2016). This code employs a rheological model more consistent with the observed deformation of geologic materials, where the response of the material is elastic on short time scales, viscous on long time scales, and with plastic failure for stresses higher than the depth-dependent cohesion of the material. See Chapter II methods for a more detailed discussion.

For each simulation, we begin with the construction of a finite element mesh, which contains between 5000 and 15000 elements. Our initial meshes are a two-layer axisymmetric mesh, approximating an unwrapped version of one-hemisphere of Mercury. This planar approximation does not include membrane lithospheric resistance, and we will discuss the implications later. We set the size of the mesh to be 3,835 km (¼ the circumference of Mercury) wide and 500 km deep (the depth of the mantle). The upper 100 km is composed of crustal material, which is based on the lithospheric support of long wavelength topography (Nimmo, 2002). The remaining 400 km of the mesh is composed of mantle material. Mesh resolution in the crust is 25 km horizontal and 10 km vertical. The mantle has a similar resolution, but a small vertical bias is applied to decrease resolution in the deep mesh away from the primary deformation in the lithosphere.

Unstable deformation (e.g., folding) amplifies existing perturbations. Thus in order to break the lateral homogeneity of the mesh, a small (10 m amplitude) harmonic perturbation in surface topography is applied, coupled with several scenarios for the crust-mantle boundary: fully compensated (Airy), flat, and uniform crustal thickness (Figure 3). We test a range of wavelengths in order to identify the fastest-growing, dominant wavelength. In our axisymmetric system that approximates an unwrapped half of Mercury, our applied perturbations are equivalent to the even number zonal spherical harmonics at degrees 6-24. For reference, the observed long-wavelength topography on Mercury (~1000 km) is equivalent to roughly degree 14.

Thermal Solution:

Each scenario requires 2 simulations, a thermal one (to set the temperature structure) and a mechanical one. For the thermal simulations, we test three different thermal cases: a constant surface temperature of 440 K and surface heat flows of 6, 25, and 40 mW m^{-2}, which bound the range of expected values for Mercury (Watters et al., 2002; Nimmo and Watters, 2004). We assumed that the thermal system is time independent and do not consider secular cooling. The thermal conductivity of the crust and mantle are 2.5 and 4 W m^{-1} K^{-1}. The heat fluxes at the sides of the mesh are set to zero.

Mechanical Solution:

Planetary contraction is simulated by a forced lateral displacement of the outer vertical boundary. We assume that the shortening that is associated with planetary contraction is equivalent to a change in planetary radius of 1 km (surface strain of 0.026 %) every 100 Myr, with a total run time of 300 Myr. This strain rate is slightly elevated as compared to the expected value. This choice was made because we assumed that the rate of volume change was higher initially and wanted to test the influence of higher strain rates. This contraction results in the formation of a lithosphere whose thickness is largely governed by the thermal state. The inner vertical boundary is free-slip, as is the base. The crustal density is 2900 kg m^{-3}, and the mantle density was 3200 kg m^{-3}. A vertical gravitational body force with an acceleration of 3.7 m s^{-2} (Mercury surface gravity) is applied to the entire mesh. The gravity causes the material in the mesh to compact slightly. To counter this self-compaction, the mesh is seeded with an initial stress that is equivalent to the overburden stress.

As previously stated above we, assume an elastic-viscous-plastic rheology. The nominal elastic Young's moduli for the crust and mantle are 65 and 140 GPa, respectively. The Poisson's ratios for both are 0.25. We apply the viscous rheologies of dried Columbia diabase for the crustal material (Mackwell et al., 1998; Nimmo, 2002) and dried olivine for the mantle materials (Karato and Wu, 1993). The time steps in the simulation are governed by the minimum Maxwell time, which is dependent upon the elastic moduli and viscosity. Higher temperatures result in lower the viscosity, which yields smaller time steps and thus increases simulation time. To keep the computational time tractable, we set the minimum viscosity to 10^{19} Pa s, and we have tested that our results are not sensitive to this choice. Plasticity was incorporated into our simulations, but had no influence on the scale of amplification, because the stress magnitudes were too low.

In these simulations, we implement a full large strain formulation, despite the low strain environment. This formulation incorporates the second-order term of the strain-displacement relationship (e.g., Ranalli, 1995), as well as a continual update to the mesh geometry. Additionally, we apply a constant dilatation scheme that controls numerical errors that yield over-stiff elements while simulating nearly incompressible behavior (e.g., viscous creep).

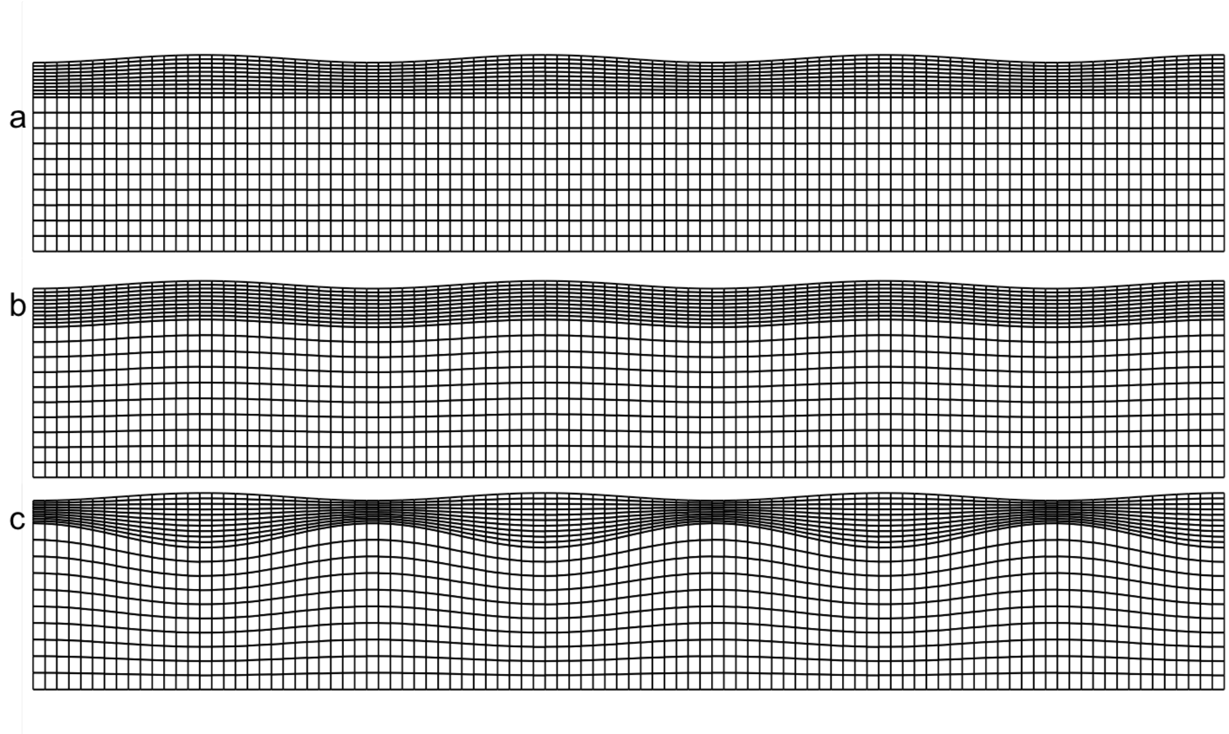

Figure 2: Schematics of the three different mesh geometries that were used (actual element sizes are much smaller). There is vertical exaggeration of 100x in order to demonstrate the shape of the initial amplitude. All of the meshes that are shown are for the degree-14 harmonic. (a) Uncompensated crust. (b) Uniform thickness crust. (c) Fully compensated crust 'Airy Isostasy.'

D. Results:

Our study demonstrates the lack of a role that folding plays in the formation of the long-wavelength topography on Mercury. For each of our 90 simulations (permutations of heat flow [3 cases], wavelength [10 cases], and scenario for the crust-mantle boundary [3 cases]), we calculate the amplification factor as a ratio of the final to initial surface topographic amplitudes. In the majority of our simulations (82/90), no positive amplification was observed (amplification < 1). In eight of our simulations, the amplification was only marginally greater than one (1.01-1.07). These simulations are for the spherical harmonic degrees 10-24 with fully compensated initial topography and a heat flow of 6 mW m^{-2}, with peak amplification occurring at the degree-12 harmonic (Fig. 3). In these simulations each subsequent time increment marginally increases the amplification (~ 1 %). On the other hand, the other values for the heat flow produce no simulations that show any positive amplification (e.g., Fig. 4). In addition, the amount of amplification decreases with increasing amounts of horizontal shortening. Fig. 3 and Fig. 4 show shortenings of 1, 2, and 3 km for a total run time of 300 Mya, which each km of deformation representing 100 Myr.

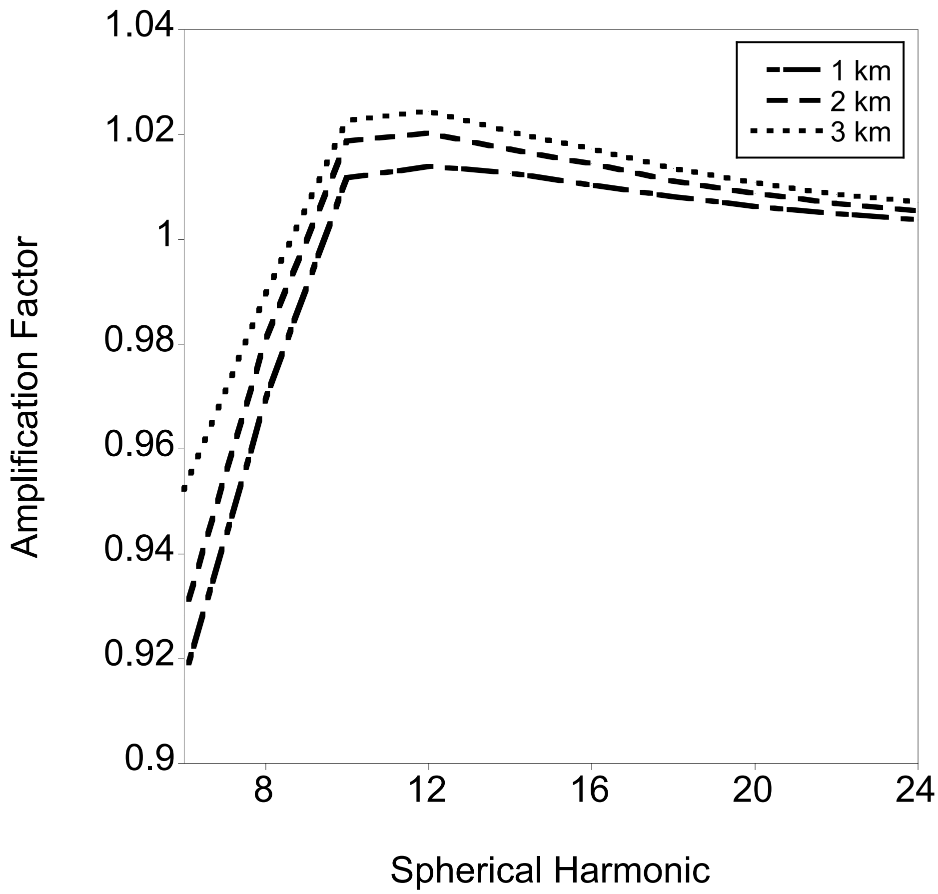

Figure 3: Amplification profiles for spherical harmonic degrees 6-24 with fully compensated topography and a heat flow of 6 mW m^{-2}. Dashed lines represented 1, 2, 3 km of horizontal shortening.

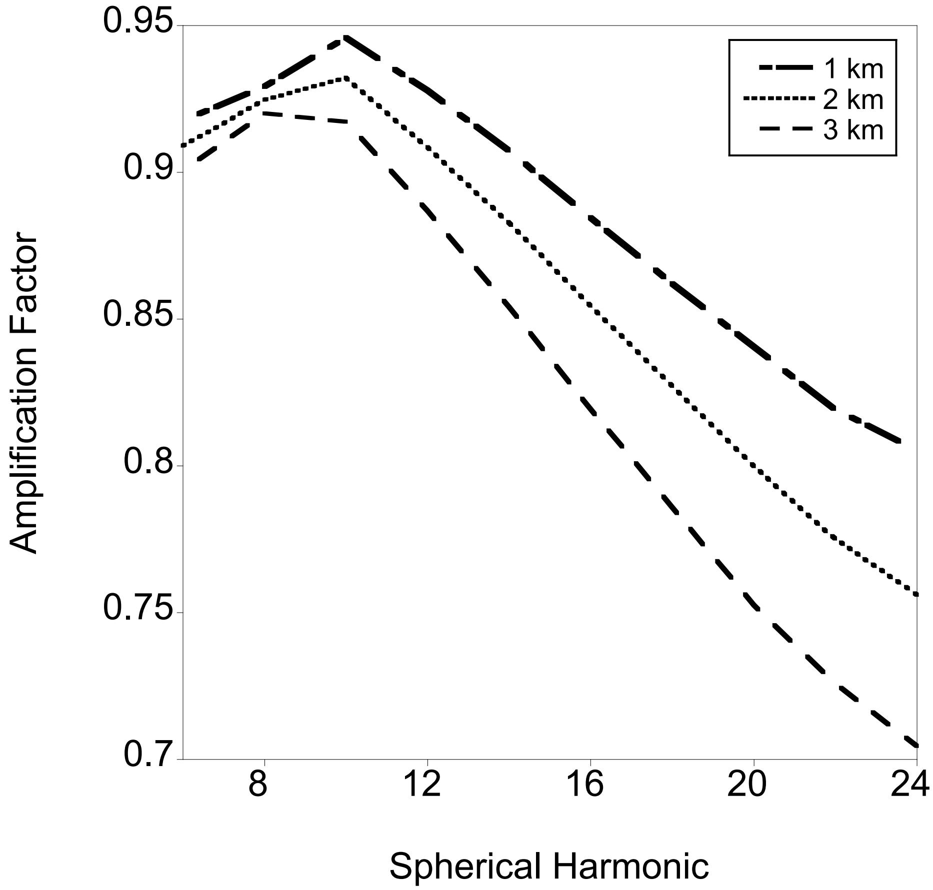

Figure 4: Amplification profiles for spherical harmonic degrees 6-24 with fully compensated topography and a heat flow of 40 mW m^{-2}. Dashed lines represented 1, 2, 3 km of horizontal shortening.

For full results of the simulations, see Appendix D. Simulations that were run with a higher initial amplitude (100 m) yielded amplification values that were within 0.1 %. We also found that amplification was large invariant of time. This was tested by running simulations with the same amount of deformation but with the time for each km both halved (50 Myr) and doubled (200 Myr).

E. Discussion:

The presence of long-wavelength topography on Mercury has been both hypothesized about (Dombard et al., 2001) prior to MESSENGER and found by the mission (Balcerski et al., 2012; Klimczak et al., 2013b; Watters et al., 2016). The formation of this topography, however, does not appear to be the result from folding of the lithosphere due to contraction of the lithosphere that resulted from the cooling of Mercury. Our results demonstrate that an origin for the long wavelength topography on Mercury via lithospheric folding is unlikely, in contrast to the predictions from semi-analytic models using a more simplistic rheology. Amplifications using this more realistic rheology are significantly lower, consistent with recent work exploring periodic topography in the outer solar system (e.g., Bland et al., 2015). The elastic-viscous-plastic rheology provides additional component for accommodations of stress (i.e., elasticity) as compared to previous work, which tends to reduce fold amplitudes. The inclusion of planetary curvature would exacerbate this issue, because the membrane response of the lithosphere would further resist folding.

Notably, we find only (minor) positive amplification for the case of a low heat flow and with a crust in full Airy isostasy. Simulations that started out of isostatic equilibrium (the surface topographic perturbation underlain by either a flat or matching crust-mantle boundary) all saw rapidly decreasing amplitudes of surface topography, indicating that any folding instability is overwhelmed by a collapse towards isostasy. Simulations that started in compensation do see amplification, but only for the lowest heat flow considered (i.e., the thickest, strongest lithosphere). These simulations at higher heat flow again do not amplify because of the tendency towards isostasy with the weaker lithosphere. In these simulations the base of the crust has undergone the same amount of amplification as the surface. This implies that the initial perturbation of the crust is no longer supported isostatically and is now solely supported by the crust. As the heat flow increases in our simulations and the total amount of amplification decreases the ability of the lithosphere to support the initial perturbation decreases.

Indeed, our low amplification factors imply a kilometer scale perturbation to yield the observed 3 km of topographic amplitude, which is of course unlikely; had the initial topography been of that scale, then there would be no need to invoke folding. The resolution to this paradox in the outer solar system is to necessitate larger amounts of horizontal shortening (levels > 10%) in order to amplify a reasonable perturbation into observable topography (e.g., Bland et al., 2015). We test some of our simulations with significantly higher degrees of shortening (10%) at much higher strain rates (though we find little sensitivity to strain rate). We have found much greater amplification (~10 times), but there is no physical evidence or theoretical reason for Mercury to have shrunk by the requisite 244 km needed for this degree of horizontal shortening. Indeed, full solidification of Mercury's core would only yield a radius change of ~17 km (Solomon, 1975).

G. Conculsion:

These results imply that there must be an alternative mechanism for the formation of the observed long-wavelength topography within and around Caloris. For this work we have tested every plausible situation under which the lithosphere of Mercury could have folded due to contraction. This has included a range of thermal conditions, altering the support of the topography, changing the strain rate, using alterative rheology's for the crust, and testing different viscosities. The most direct implication of our results is that the decreasing amplitudes of all cases except for the lowest heat flow under initial compensation, including the near complete collapse of our constant crustal thickness scenarios, indicate that the lithosphere of Mercury cannot support topography at this horizontal scale without buoyant support. Indeed, the observed gravity anomalies of Mercury are consistent with isostatic support of this topography (James et al., 2015). Thus, future work should be directed at understanding mechanisms to produce compensated high topography at large horizontal scales. To end on pure speculation, we suggest extensive magmatic thickening of the crust over sheet-like convective upwellings in the mantle.

H. References:

Balcerski, J.A., Hauck, S.A., Sun, P., Klimczak, C., Byrne, P.K., Dombard, A.J., Barnouin, O.S., Zuber, M.T., Phillips, R.J., Solomon, S.C., 2012. Tilted Crater Floors: Recording the History of Mercury's Long-Wavelength Deformation. Presented at the Lunar and Planetary Science Conference, p. 1850.

Bland, M.T., McKinnon, W.B., Schenk, P.M., 2015. Constraining the heat flux between Enceladus' tiger stripes: Numerical modeling of funiscular plains formation. Icarus 260, 232–245. doi:10.1016/j.icarus.2015.07.016

Byrne, P.K., Klimczak, C., Celâl Şengör, A.M., Solomon, S.C., Watters, T.R., Hauck, I.I.S.A., 2014. Mercury/'s global contraction much greater than earlier estimates. Nat. Geosci. 7, 301–307. doi:10.1038/ngeo2097

Dombard, A.J., Hauck II, S.A., 2008. Despinning plus global contraction and the orientation of lobate scarps on Mercury: Predictions for MESSENGER. Icarus 198, 274–276. doi:10.1016/j.icarus.2008.06.008

Dombard, A.J., Hauck, S.A., Solomon, S.C., Phillips, R.J., 2001. Potential for Long-Wavelength Folding on Mercury, in: Lunar and Planetary Science Conference. Presented at the Lunar and Planetary Science Conference.

Dombard, A.J., McKinnon, W.B., 2006a. Elastoviscoplastic relaxation of impact crater topography with application to Ganymede and Callisto. J. Geophys. Res. Planets 111, E01001. doi:10.1029/2005JE002445

Dombard, A.J., McKinnon, W.B., 2006b. Folding of Europa's icy lithosphere: an analysis of viscous-plastic buckling and subsequent topographic relaxation. J. Struct. Geol., Faulting and fault-related processes on planetary surfaces 28, 2259–2269. doi:10.1016/j.jsg.2005.12.003

Hauck II, S.A., Dombard, A.J., Phillips, R.J., Solomon, S.C., 2004. Internal and tectonic evolution of Mercury. Earth Planet. Sci. Lett. 222, 713–728. doi:10.1016/j.epsl.2004.03.037

Head, J.W., Murchie, S.L., Prockter, L.M., Robinson, M.S., Solomon, S.C., Strom, R.G., Chapman, C.R., Watters, T.R., McClintock, W.E., Blewett, D.T., Gillis-Davis, J.J., 2008. Volcanism on Mercury: Evidence from the First MESSENGER Flyby. Science 321, 69–72. doi:10.1126/science.1159256

James, P.B., Zuber, M.T., Phillips, R.J., Solomon, S.C., 2015. Support of long-wavelength topography on Mercury inferred from MESSENGER measurements of gravity and topography. J. Geophys. Res. Planets 120, 287–310. doi:10.1002/2014JE004713

Karato, S., Wu, P., 1993. Rheology of the Upper Mantle: A Synthesis. Science 260, 771–778. doi:10.1126/science.260.5109.771

Karimi, S., Dombard, A.J., 2016. On the possibility of viscoelastic deformation of the large south polar craters and true polar wander on the asteroid Vesta. J. Geophys. Res. Planets 121, 2016JE005064. doi:10.1002/2016JE005064

Karimi, S., Dombard, A.J., Buczkowski, D.L., Robbins, S.J., Williams, R.M., 2016. Using the viscoelastic relaxation of large impact craters to study the thermal history of Mars. Icarus 272, 102–113. doi:10.1016/j.icarus.2016.02.037

Klimczak, C., Ernst, C.M., Byrne, P.K., Solomon, S.C., Watters, T.R., Murchie, S.L., Preusker, F., Balcerski, J.A., 2013a. Insights into the subsurface structure of the Caloris basin, Mercury, from assessments of mechanical layering and changes in long-wavelength topography. J. Geophys. Res. Planets 118, 2030–2044. doi:10.1002/jgre.20157

Klimczak, C., Ernst, C.M., Byrne, P.K., Solomon, S.C., Watters, T.R., Murchie, S.L., Preusker, F., Balcerski, J.A., 2013b. Insights into the subsurface structure of the Caloris basin, Mercury, from assessments of mechanical layering and changes in long-wavelength topography. J. Geophys. Res. Planets 118, 2030–2044. doi:10.1002/jgre.20157

Mackwell, S.J., Zimmerman, M.E., Kohlstedt, D.L., 1998. High-temperature deformation of dry diabase with application to tectonics on Venus. J. Geophys. Res. Solid Earth 103, 975–984. doi:10.1029/97JB02671

Melosh, H.J., McKinnon, W.B., 1988. The tectonics of Mercury, in: Mercury, University of Arizona Press. pp. 374–400.

Nimmo, F, 2002. Constraing the crustal thickness on Mercury from Viscos topographic relaxation. Geophys. Res. Lett. 29, 7-1

Nimmo, F., Watters, T.R., 2004. Depth of faulting on Mercury: Implications for heat flux and crustal and effective elastic thickness. Geophys. Res. Lett. 31, L02701. doi:10.1029/2003GL018847

Smith, D.E., Zuber, M.T., Phillips, R.J., Solomon, S.C., Hauck, S.A., Lemoine, F.G., Mazarico, E., Neumann, G.A., Peale, S.J., Margot, J.-L., Johnson, C.L., Torrence, M.H., Perry, M.E., Rowlands, D.D., Goossens, S., Head, J.W., Taylor, A.H., 2012. Gravity Field and Internal Structure of Mercury from MESSENGER. Science 336, 214–217. doi:10.1126/science.1218809

Solomon, S.C., 1976. Some aspects of core formation in Mercury. Icarus 28, 509–521. doi:10.1016/0019-1035(76)90124-X

Solomon, S.C., Klimczak, C., Byrne, P.K., Hauck, S.A., Balcerski, J.A., Dombard, A.J., Zuber, M.T., Smith, D.E., Phillips, R.J., Head, J.W., Watters, T.R., 2012. Long-Wavelength Topographic Change on Mercury: Evidence and Mechanisms. ResearchGate 43, 1578.

Strom, R.G., Trask, N.J., Guest, J.E., 1975. Tectonism and volcanism on Mercury. J. Geophys. Res. 80, 2478–2507. doi:10.1029/JB080i017p02478

Watters, T.R., Montési, L.G.J., Oberst, J., Preusker, F., 2016. Fault-bound valley associated with the Rembrandt basin on Mercury. Geophys. Res. Lett. 43, 2016GL070205. doi:10.1002/2016GL070205

Watters, T.R., Robinson, M.S., Bina, C.R., Spudis, P.D., 2004. Thrust faults and the global contraction of Mercury. Geophys. Res. Lett. 31, L04701. doi:10.1029/2003GL019171

Watters, T.R., Robinson, M.S., Cook, A.C., 1998. Topography of lobate scarps on Mercury: New constraints on the planet's contraction. Geology 26, 991–994. doi:10.1130/0091-7613(1998)026<0991:TOLSOM>2.3.CO;2

Watters, T.R., Schultz, R.A., Robinson, M.S., Cook, A.C., 2002. The mechanical and thermal structure of Mercury's early lithosphere. Geophys. Res. Lett. 29, 37–1. doi:10.1029/2001GL014308

Watters, T.R., Solomon, S.C., Robinson, M.S., Head, J.W., André, S.L., Hauck II, S.A., Murchie, S.L., 2009. The tectonics of Mercury: The view after MESSENGER's first flyby. Earth Planet. Sci. Lett., MESSENGER's First Flyby of Mercury 285, 283–296. doi:10.1016/j.epsl.2009.01.025

Zuber, M.T., Smith, D.E., Phillips, R.J., Solomon, S.C., Neumann, G.A., Hauck, S.A., Peale, S.J., Barnouin, O.S., Head, J.W., Johnson, C.L., Lemoine, F.G., Mazarico, E., Sun, X., Torrence, M.H., Freed, A.M., Klimczak, C., Margot, J.-L., Oberst, J., Perry, M.E., McNutt, R.L., Balcerski, J.A., Michel, N., Talpe, M.J., Yang, D., 2012. Topography of the Northern Hemisphere of Mercury from MESSENGER Laser Altimetry. Science 336, 217–220. doi:10.1126/science.1218805

CHAPTER IV

IV. SIMULATING SPATIAL VARIATIONS OF LITHOSPHERIC FOLDING IN THE SOUTH POLAR TERRAIN OF ENCELADUS

Chapter IV will be submitted to Icarus as:

Jonathan P. Kay[1] and Andrew J. Dombard[1]

1 - The Department of Earth and Environmental Sciences (MC-186), University of Illinois at Chicago, 845 W. Taylor St., Chicago, IL 60607, USA.

A. Abstract:

The South Polar Terrain (SPT) of Saturn's moon Enceladus is a young, heavily lineated region that has been shown to be in the act of active cryovolcanic venting. A set of roughly evenly spaced, subparallel fissures, collectively known as the Tiger Stripes, cut across the SPT and is the source of the venting. Additionally, thermal observations demonstrated anomalously high heat flow coming out of the whole SPT in general, and the Tiger Stripes in particular; total heat power out of the region has been estimated to be ~5-18 GW, more than what can be supplied by equilibrium tidal heating and suggesting temporal variability in the thermal structure of the SPT. Between the Tiger Stripes are a series of closely spaced, short wavelength (1.1 km) linear features generally following the trend of the Tiger Stripes, which has been interpreted as folding of a surface layer undergoing compression. In addition, periodic ridges and troughs (5 km wavelength) found in the zone rimming the SPT have been interpreted recently as contractional features. Here, we simulate the formation of both types in order to constrain the thermal conditions required for their formation. Reproducing the shorter wavelength features necessitates high surface temperatures (185 K) and high heat flows (400 mW m^{-2}), results consistent with past work. The long wavelength features need lower surface temperatures (130 K) and heat flows (100 mW m^{-2}), which demonstrates a spatial variability heat lost from the center to the periphery of the SPT.

B. Introduction:

Enceladus's geologic activity is focused within the South Polar Terrain (SPT), which consists of young (less than 1 Myr), tectonically disrupted terrain that is separated from the rest of the moon by a distinct boundary of sub-parallel ridges and troughs hundreds of meters high (Porco et al., 2006; Beddingfield et al., 2013). The most striking feature within the SPT is the long, parallel fractures known as "tiger stripes" (Porco et al., 2006), and the mostly water ice plumes that supply Saturn's E-ring originate from these stripes (Porco et al., 2006). Additionally, thermal measurements from the Composite Infrared Spectrometer (CIRS) instrument on Cassini revealed temperatures > 180 K, far in excess of the expected surface temperature of ~75 K (Spencer et al., 2006), suggesting elevated regional heat flow; the highest temperatures are associated with the tiger stripes, further implicating these unique features as loci of activity. Integrating this excess temperature over the SPT, the total emitted power has been estimated to be 5.8 to 18.9 GW (Spencer et al., 2006; Howett et al., 2011). Several proposals have been made that attempt to explain this regional heat source: tidal heating due to the diurnal bulge (Porco et al., 2006; Spencer et al., 2006; Meyer and Wisdom, 2007; Roberts and Nimmo, 2008), a forced libration due to its non-spherical shape (Hurford et al., 2009), decomposition of clathrate due to degassing through the pervasively fractured lithosphere (Kieffer et al., 2006), or by tidally driven lateral (strike- slip) fault motion (frictional shear heating) (Nimmo et al., 2007).

Other than the tiger stripes, the main landform found in the SPT is sub-parallel to parallel ridges and troughs. These include those that strike roughly parallel to the boundary at ~55° S latitude between the SPT and the rest of Enceladus, which have wavelengths of ~5 km and amplitudes of several hundred meters. Similarly, high-resolution images of the south pole of Enceladus have revealed regions of closely spaced quasi-linear features that exist between the tiger stripes and possess a wavelength of ~1.1 km. These ridges are mostly linear to sub-linear and in general run parallel to the tiger stripes and will often follow their orientation. In some cases they can intersect with other ridges, but can run up to tens of km along the strike of the trough. Barr and Preuss (2010) thought the terrain looked similar to the ropy pahoehoe commonly found on terrestrial basaltic lava flows, and hence dubbed it "ropy" terrain.

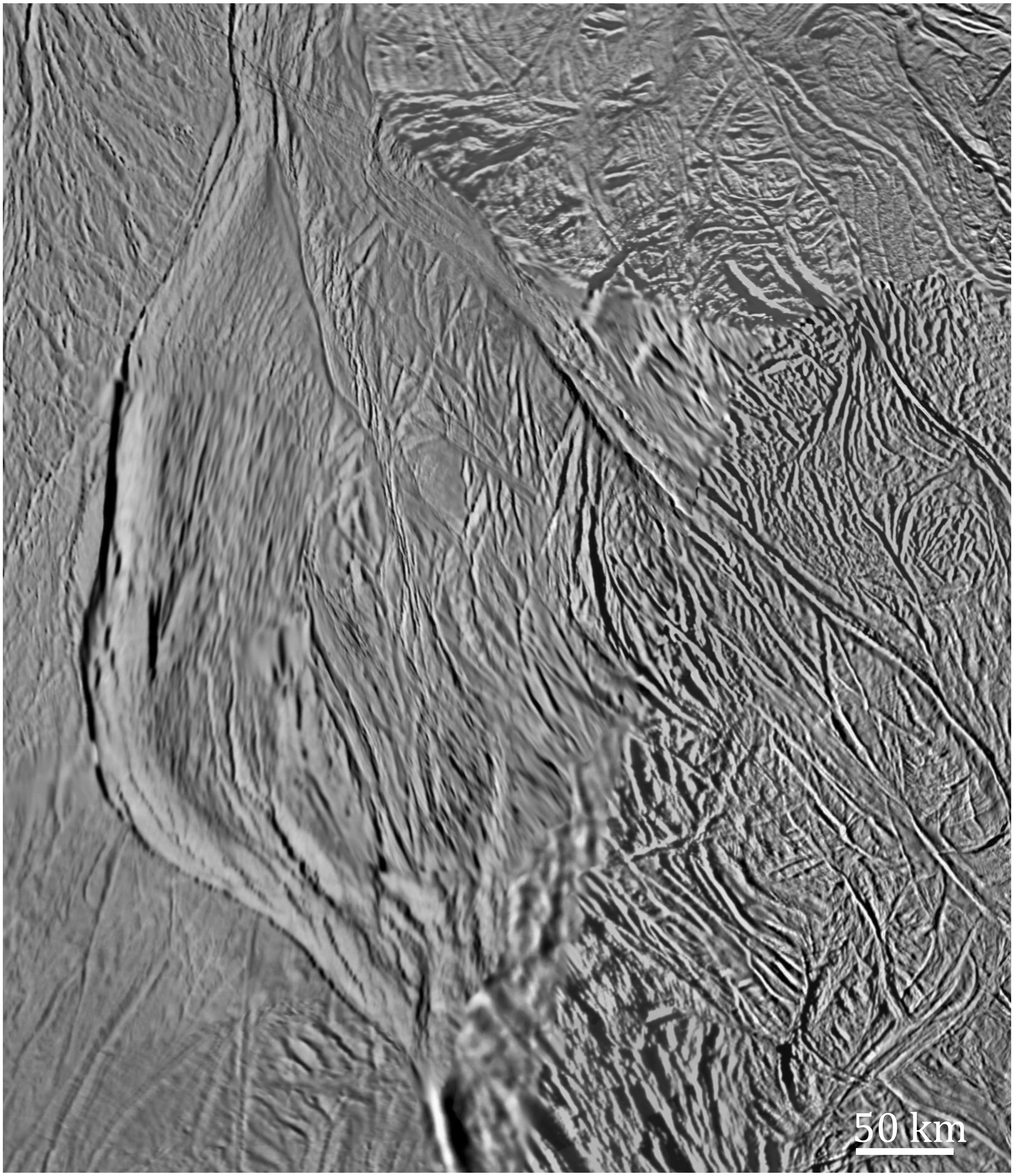

Figure 1: Close up view of Edge of SPT. PIA12566. This is an example of the long wavelength features as in Beddingfield et al., (2013).

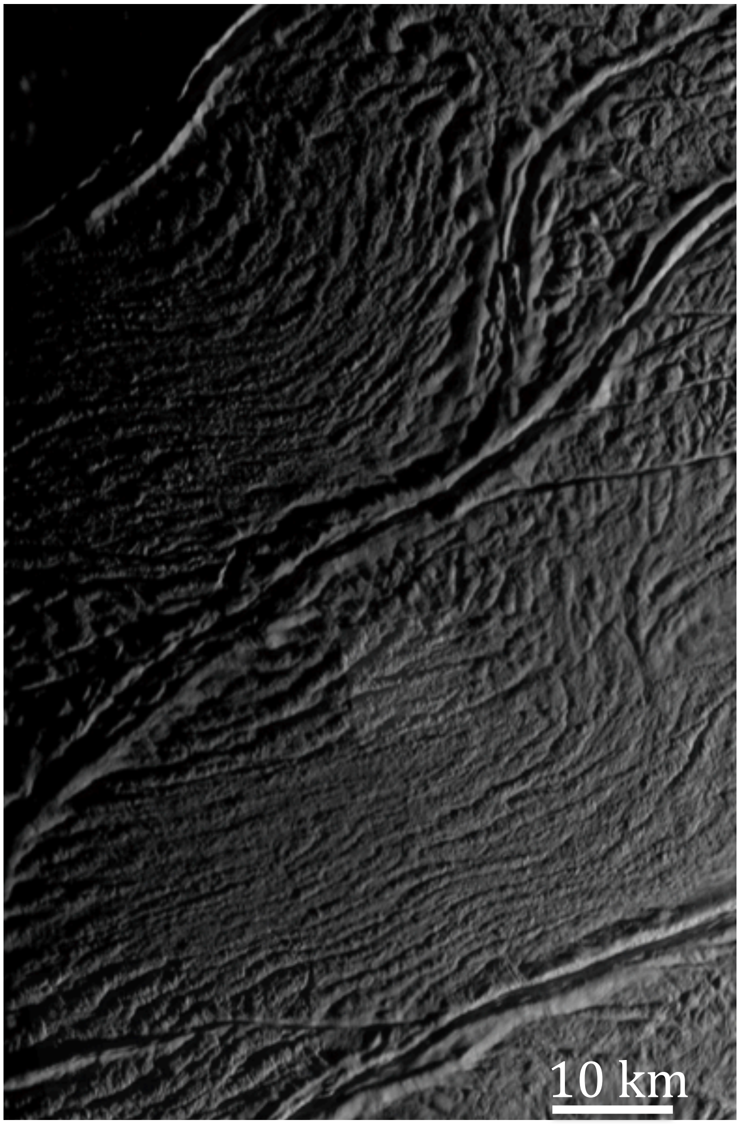

Figure 2: Close up view of SPT. This shows the short wavelength features between the tiger stripes (arrows).

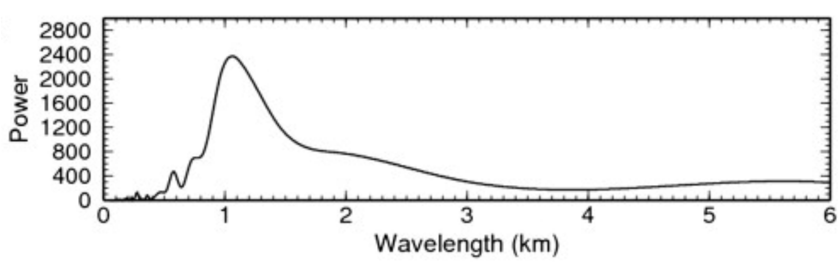

Figure 3: Results of a spectral analysis of the ropy terrain between the tiger strips, showing a dominant wavelength of ~1.1 km. Adapted from Barr and Preuss [2010].

The ridges and troughs both in between the tiger stripes and along the boundary of the SPT have been interpreted as forming in response to local compressive stresses. The sub-parallel ridges and troughs in the SPT boundary zone have slopes and changes in slopes that have suggested a contractional formation mechanism, potentially folding of a lithosphere (Beddingfield et al., 2013). These authors applied a geometric analysis to elevation models of the features to estimate the amount of horizontal shortening at a minimum of 10%. Recent numerical work has revealed, however, that substantial shortening of an icy lithosphere can be taken up largely by passive thickening during the incipient nucleation stage of a lithospheric fold; consequently, strain estimates based on the geometry of putative long-wavelength, low-amplitude folds significantly under-predicted the amount of horizontal shortening (Bland and McKinnon, 2012). Understanding how much shortening these folds accommodate is critical to unraveling the mechanical history of the SPT.

Between the tiger stripes, the pahoehoe texture believed to be analogous to ropy terrain forms under a compressional stress acting on the colder (more viscous) surface layer of the lava, causing folding (Fink and Fletcher, 1978; Fink, 1980; Barr, 2008; Bland et al., 2015). Thus, Barr and Preuss (2010), employing a semi-analytic model with a purely viscous rheology (Fink, 1980), constrained the conditions during folding, namely thickness of the folding layer consistent with the observed wavelength and compressive stress magnitudes needed to overcome the resistive weight of a growing fold. However, this work did not resolve the growth of the folds to their observed amplitude because it employed small strain theory and used a simple viscous rheology (Fink and Fletcher, 1978; Fink 1980). Subsequent work, taken to large strains and using a more realistic rheology found an extremely narrow parameter space in which it was possible to form this short-wavelength topography (Bland and McKinnon, 2012).

Thus, these two scales of putative folds present an opportunity. Wavelength scales with the thickness of the folding layer, and for lithospheric folds, this thickness primary depends on thermal state. Consequently, understanding the formation of these two scales of folds may allow constraints on the variation of the thermal state between the center of the SPT and its boundary. Such an assessment can be used to refine estimates of the thermal power emitting from the SPT and further elucidate the engine that is driving the perplexing activity on Enceladus. Our goal with this work is to use a more sophisticated rheology in finite element simulations of lithospheric contraction to confirm a folding origin and to constrain the thermal and mechanical conditions needed for this mechanism, with implications for the evolution of the SPT. In addition, this would should be able to estimate of at least constrain the total strain that has occurred between the Tiger Stripes and the amount of strain along the boundary of the SPT.

C. Methods:

We use the commercially available MSC.Marc finite element package. The software is well suited to the investigation of geodynamic problems (e.g., Dombard and McKinnon, 2006a, 2006b; Dombard and Cheng, 2008; White et al., 2013). We use material, thermal, and rheological parameters for water ice. We apply an ice density of 950 kg m^{-3}, and use a temperature dependent thermal conductivity of $651/T$ (Petrenko and Whitworth, 1999). The rheology is elastic-viscous-plastic. For the elasticity, we adopt the values measured by Gammon et al. (1983): a Young's Modulus of 9.332 GPa and a Poisson's Ratio of 0.3252.

The viscous rheology of ice at planetary conditions has been measured (e.g., Goldsby and Kohlstedt, 2001), and it is complex and non-Newtonian. Past work looking at putative folds in the SPT (Barr and Preuss 2010; Bland et al., 2015) linearized this viscous rheology to a Newtonian flow law that was temperature-dependent:

$$\eta = \eta_0 e^{l\left(\frac{T_m}{T}-1\right)}, \qquad (1)$$

where T is the temperature, η_0 is the reference viscosity for ice at the melting temperature T_m (273 K), and the constant l is $E/RT_m = 26$, where R is the gas constant and with an activation energy $E = 60$ kJ mol^{-1} 1 (dislocation creep of ice I (Goldsby and Kohlstedt 2000; Durham et al., 2010)). This viscosity structure captures the dominating temperature behavior of ice, but not the stress dependence. To build upon this past work and facilitate comparison of results, we adopt this linearized flow law here. Incorporating the stress dependence to the ice rheology remains for future work.

Following standard geodynamical modeling techniques, we model the brittle behavior as time-independent, permanent plastic deformation, with a linear Mohr-Coulomb yield criterion constrained by a "Byerlee's rule" for ice (Beeman et al. 1988). Following Bland (Bland et al., 2015), we also adopt a strain weakening mechanism to simulate the weakening effects of fault gouge with progressive slip along faults in the brittle lithosphere.

Our simulated domain is one radial slice in a planar geometry, as the folds are largely invariant along their strike for distances far longer than the wavelengths. We test for both the shorter wavelength features (~1.1 km) and the longer wavelength features (~5 km). Taking advantage of symmetry, we simulate a crest to trough of an initial sinusoidal topographic perturbation of 1 m in amplitude, thereby looking at each wavelength independently. For each mesh. We set the depth of the domain to be equal to twice the width of the mesh. In lithospheric folding, all wavelengths can grow (or even shrink), but one dominant wavelength grows faster than all others, which is the wavelength that ultimately is amplified enough to be observed (Dombard and McKinnon, 2006a). To identify the dominant wavelength of folding between the tiger stripes, 19 different widths were tested: 600, 650, 700, 750, 800, 850, 900, 950, 1000, 1050, 1100, 1150, 1200, 1250, 1300, 1350, 1400, 1450, 1500 m. This values are half-wavelengths, meaning that the initial wavelengths that we consider are uniformly longer than the ~1.1 km spacing seen in between the SPT. Recent work, however, has highlighted that unstable lithospheric deformation (i.e., folding in contraction) requires lateral displacements in excess of 10% (Bland et al., 2015). Thus, these initial wavelengths will be compressed with progressive folding, and matching the initial dominate wavelength with the amount of horizontal shortening is one of our goals. For the longer wavelength boundary folds, 12 mesh widths are tested. We set the depth to be twice the width of the mesh and the widths to be 2500, 3000, 3500, 4000, 4500, 5000, 5500, 6000, 6500, 7000, 8000, and 9000 m.

The thickness of the lithosphere will largely be a product of the thermal structure in the subsurface. We first perform a series of steady-state thermal simulations to determine the temperature field, and the results of the thermal simulations are piped into the corresponding mechanical simulations. For our initial thermal simulations, we solve for the steady state equilibrium between a fixed surface temperature and a constant applied basal heat flux (and assume zero heat flux on the mesh sides). We consider a range of basal heat fluxes of 100 - 400 mW m^{-2}, which brackets the expected heat flow out of the SPT during this epoch (Spencer et al., 2006; Howett et al., 2011). In addition, we tested a range of surface temperature values that range from 90-185 K (Spencer et al., 2006; Howett et al., 2011).

For these simulations, we implement a full large strain formulation, which includes the second-order term of the strain displacement relationship and a geometric update. During the simulation, the mesh geometry changes continuously, and since topography is a source of stress, updating the geometry is required. Additionally, we apply a constant dilatation scheme that controls numerical errors that yield over-stiff elements while simulating nearly incompressible behavior (e.g., viscous creep). The gravity causes the material in the mesh to compact slightly. To counter this self-compaction, the mesh is seeded with an initial stress that is equivalent to the overburden stress.

We also assume a formation time scale of 1 Myr, consistent with the young crater retention age of the SPT and with the observed geologic activity. Furthermore, we presume that the features underwent a significant amount of lateral contraction and test cases out to 20% horizontal shortening, with outputs every 10%, for a rate of $\sim 10^{-14}$ s^{-1}. We apply a density of 950 kg m^{-3}, a gravity of 0.113 m s^{-2}.

For the ropy terrain (or funiscular folds) Bland et al., (2015) found that the folds required both a high heat flow (~400 mW m^{-2}) and a high surface temperature (185 K). These values are based on the CIRS data (Howett el al., 2010) and are assumed to be the maximum potential value for both the surface temperature and the heat flow. Such high surface temperatures, well above solar equilibrium, can be realized by excess heat leaving the SPT as well as an effective surface temperature arising from a blanket of very porous, low thermal conductivity ice, presumably plume fall-out (Bland et al., 2015). We seek to confirm these values for the formation of the ropy terrain between the tiger stripes. This should establish the minimum conditions required for folding within the Tiger Stripes and will allow us to further explore the formation of folds within the SPT.

D. Results:

In order to identify the dominant wavelength of the folding instability, we search for the largest amplification factor, which is defined as the ratio of topographic amplitude to its initial value (1 m for these simulations). All results shown in this section are shown after 10% shortening. Our results demonstrate different amplification scenarios for the two sets of folds, but are dependent on the surface temperature and heat flow combination that is used. In the case of high surface temperature simulations of 185 K and a high heat flow of 400 mW m^{-2} (cf. Bland et al., 2015), there is increased amplification as the half-wavelengths increase, until it reaches a half-wavelength of 1100 m (Fig. 4). This indicates that 2200 m is the dominant wavelength (i.e., fastest growing), and in order to achieve the observed wavelength (~1.1 km), 50% shortening would need to occur. None of the half-wavelengths that are tested shows much amplification for shortening less than 10%, consistent with other recent results (Bland et al., 2015). This result sets a benchmark for the lithospheric thickness (~50 m) based on the high-end values of both heat flow and surface temperature. Thus, the final wavelength predicted from these simulations will be a convolution of the lithospheric thickness set by the thermal state and the total amount of horizontal shortening.

Using this thermal state as a benchmark, we can compare the lithospheric thickness of this model to other testable models within the parameter space of heat flow and temperature ranges (Fig.5). We do this by creating a series of yield strength envelopes that plot the differential stress as a function of depth. Each of the curves have a different heat flow and temperature combination, but all of them contain large strength contrasts suggesting that folding is potentially possible in a wide range of situations.

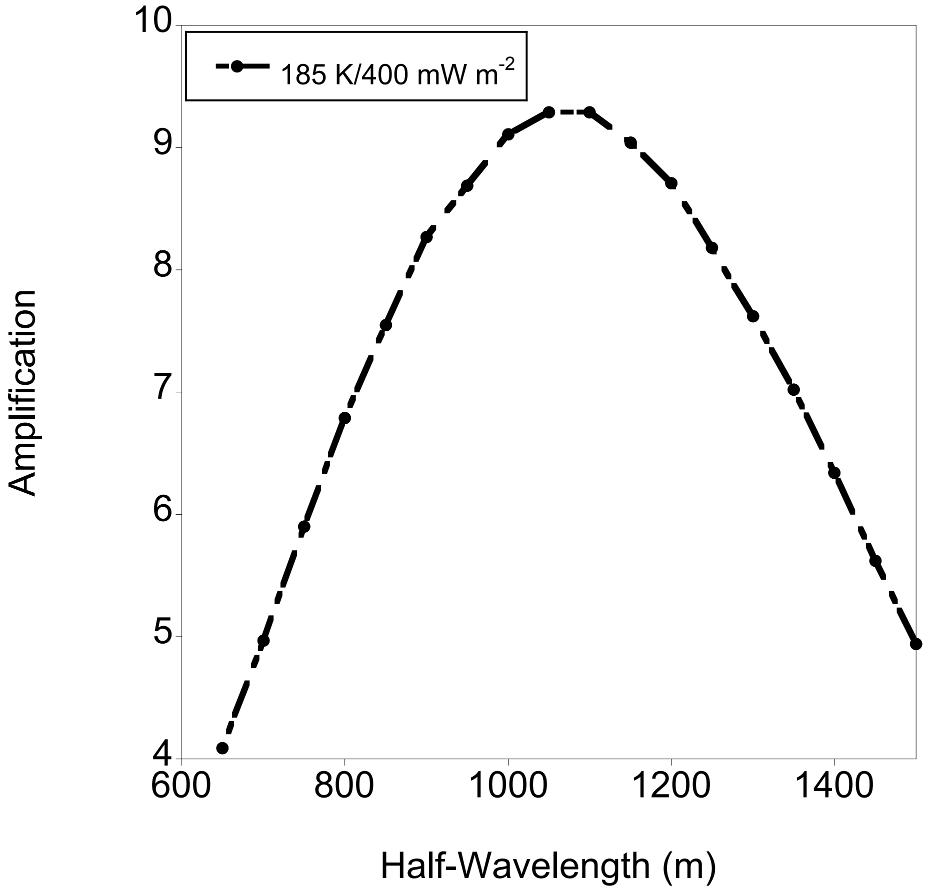

Figure 4: Amplification as a function of half-wavelength, for a surface temperature of 185 K and a heat flow of 400 mW m^{-2} (cf. Bland et al., 2015). Peak-amplification occurs at 1100 m. This situation requires 50% shortening to produce the observed wavelength.

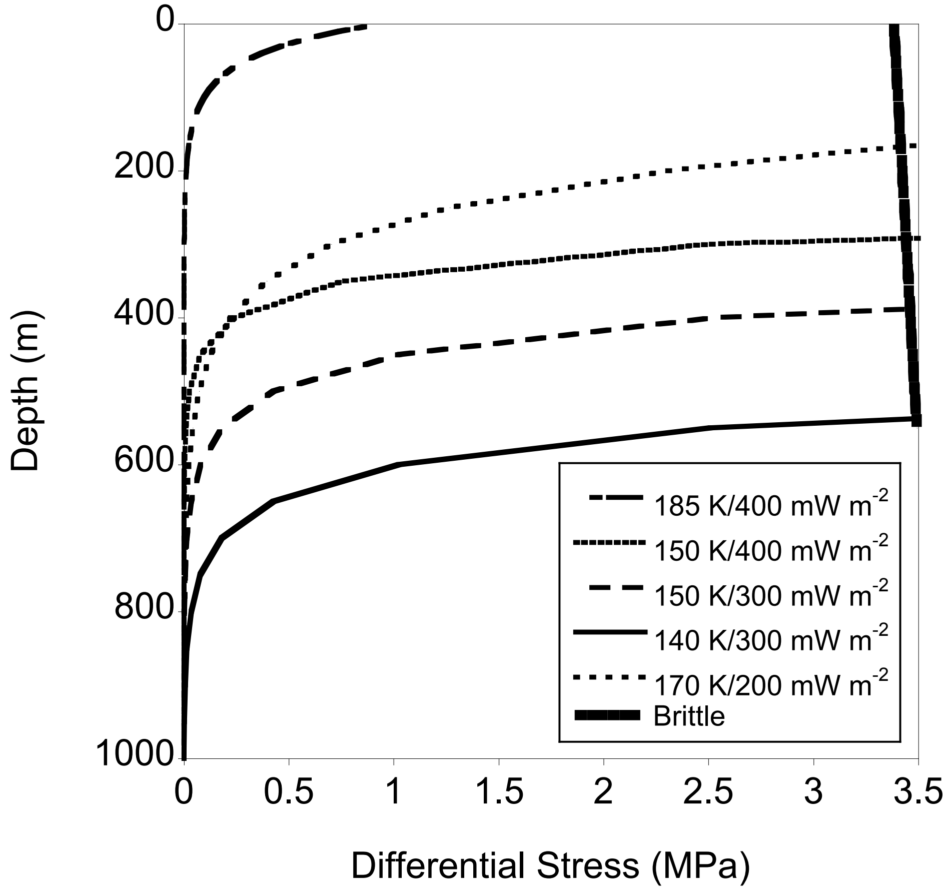

Figure 5: Differential stress as a function of depth, where each line corresponds to a specific thermal state.

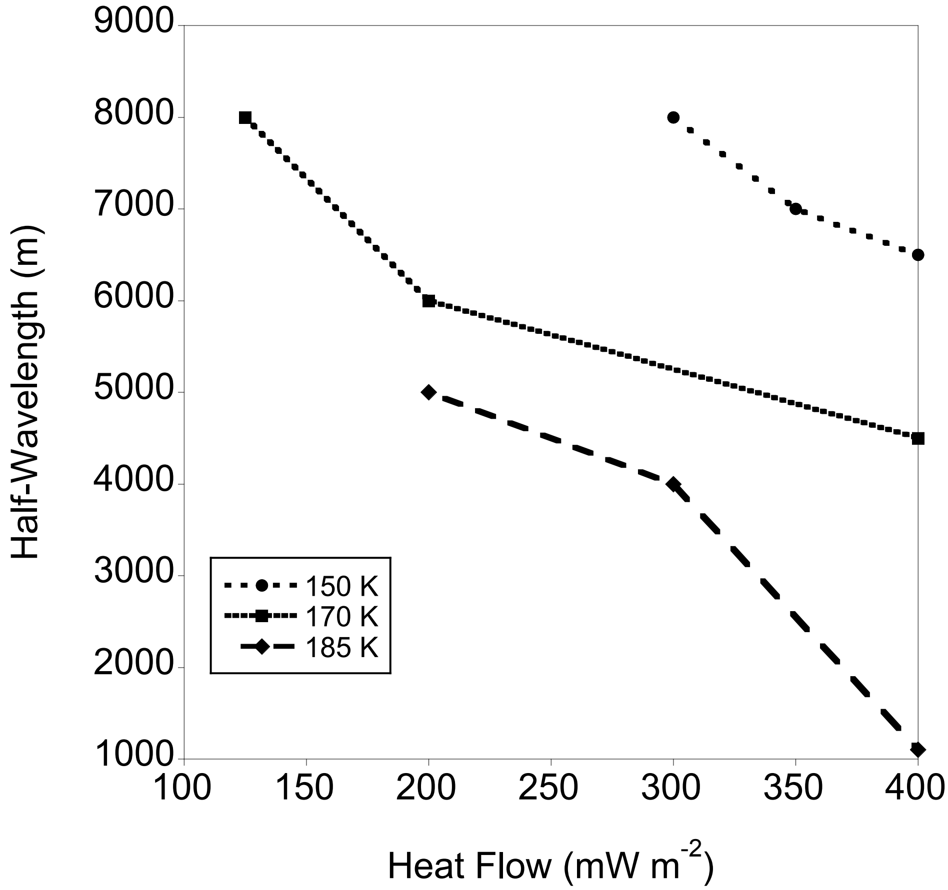

Figure 6: Heat flow and surface temperature combinations and the dominant amplification wavelength.

This then allows for the building a series of simulations that show the dominant wavelength for a given surface temperature as a function of heat flow (Fig. 6). Here, we show the initial wavelength of the fastest growing (i.e., dominant) folding instability. With progressive amounts of horizontal shortening, these initial instability wavelengths, which are generally longer than the observed topography, can be compressed to match the observations, again making the amount of shortening an important parameter. The results are summarized in Table 1.

Table 1: Reference table for results of simulation for producing the dominant amplification wavelength

Temperature (K)	Heat Flow (mW m^{-2})	Peak Half wavelength (km)	Fold Length (km)	Ropy Terrain Strain (%)	Peripheral Fold Strain (%)
150	300	8	16	93	68
150	350	7	14	92	65
150	400	6.5	13	91	60
170	125	8	16	93	68
170	200	6	12	90	60
170	400	5	10	90	50
185	200	5	10	90	50
185	300	4	8	85	37.5
185	400	1.1	2.2	50	N/A

Comparing Fig. 5 with Fig. 6, thinner lithospheres result in shorter dominant wavelengths, in agreement with past work on lithospheric instabilities (Bland et al., 2015).

E. Discussion:

Our results further justify the assumption that the terrain adjacent to the tiger stripes and along the inner border of the SPT formed via thin-skinned folding. Bland et al. (2015) was able to produce fold wavelengths that were 30% longer than the presently observed wavelength using a high surface temperature and high heat flow (cf. Fig. 4). Our results for the ropy terrain are also capable of producing the observed wavelength but require 50% more strain than the Bland et al. (2015) work. This discrepancy could potentially be explained by the lack of resolution of the lithosphere within their models. The yield strength envelope with a surface temperature of 185 K and a heat flow of 400 mW m^{-2} yields a lithosphere that is ~50 m thick (Fig. 5), exactly the thickness of their elements. Indeed, our sensitivity tests also reveal shorter dominant wavelengths when the thickness of the lithosphere is under-resolved by our finite element mesh.

Therefore, these results set a minimum benchmark for the total strain that has been accommodated within the SPT. It is likely that without crustal recycling (for which there is no evidence), the periphery folds underwent less strain that the ropy terrain. Presumably, the source of the compression is the accretion of material within the tiger stripes (Barr and Preuss, 2010; Bland et al., 2015), which would directly squeeze the region between the stripes. This strain would also need accommodation at the edge of the SPT, but it would be distributed over a much longer boundary and hence be less. Consequently, the longer wavelengths of the peripheral folds would suggest that the thermal conditions are likely cooler, and not the same (or even warmer) thermal conditions but simply a larger amount of shortening. This conclusion is supported by the trends of the lines in Fig. 6. Here, we show that as the thickness of the lithosphere increases with either a lower surface temperature or lower heat flow (or a combination of both) that the dominant wavelength migrates to a larger value.

As the lithosphere thickens amplification factor increases. There are relatively small amplification values (~10 x) for 185 K/ 400 mW m^{-2} thermal state. However, the growth rates of these curves will increase as the shortening increases and are therefore sufficient to reproduce the observed amplitude of the ropy terrain. The amplification factor increases for thicker wavelengths, but this is consistent with the larger amplitudes that are observed along the edge of the SPT. This is potentially driven by the role of plasticity within the different folding regimes. The thin lithosphere scenarios have no plasticity and a smaller strength contrast as compared to the thicker scenarios that have the full Elastic-visco-plastic rheology.

This work has identified, however, a new problem via an unconstrained value of horizontal shortening. There are as of yet no independent estimates of strain within the SPT. This work suggests that there must be large amounts of strain required to produce both sets of folded features unless the lithospheres are thinner due to even warmer conditions considered here, particularly for the ropy terrain. This scenario, however, is likely untenable for a folding instability. Figure 5 shows that at a surface temperature of 185 K and a heat flow of 400 mW m-2 (cf. Bland et al., 2015), the yield envelope never reaches the brittle failure curve, meaning that there is rapid viscous creep even at the surface. Warmer conditions to produce a thinner lithosphere (and hence shorter wavelength) would also yield a weaker lithosphere that would reduce the strength of the instability, as folding requires a strength contrast between the folding layer and the surrounding medium.

Much effort has been put in to estimating the thermal power emitted from the SPT (Spencer et al., 2006; Howett et al., 2011; Goguen et al., 2013). The measured surface temperatures are higher at or near the tiger stripes (Howett et al., 2011; Gogun et al., 2013) and decrease as the distance from the vents increases. This creates the conditions under which we have designed our thermal models and could potentially explain the variations in wavelength of the two sets of putative folds. In our simulations, we can produce amplification that is consistent with the observed conditions on Enceladus, though we have yet to identify the exact suite that reproduces the observations. The wrinkle is that the final answers are dependent not only on the thermal conditions but also the total amount of horizontal shortening accommodated by these folds. With future independent estimates of this shortening, future simulations reveal the thermal conditions that led to folding of the lithosphere. What seems certain, however, is that there is a spatial variation in thermal conditions, higher between the tiger stripes, and decreasing towards the boundary of the SPT. Under the conditions needed to explain the ropy terrain, the initial wavelengths of the folding instabilities are already shorter than the wavelengths of the peripheral folds. Cooler thermal conditions are likely to exist as you move away from the center of the SPT.

F. Conclusions:

The SPT of Enceladus is covered in terrain that is likely the result of compression induced, thin-skinned lithospheric folding. The elevated heat flows and surface temperatures that have been measured by Cassini further support this. Based on our results, we have estimated that the ropy terrain has undergone a minimum of 50% strain to achieved its present wavelength of 1.1 km. This is based on the using a heat flow (400 mW m^{-2}) and a surface temperature (185 K) that are on the high end of expected values. It is likely that both the surface temperature and heat flow values were lower, but that would push the dominant wavelength to a longer length and therefore require a larger amount of strain to produce the observed deformation. We have also shown that it is possible to reproduce the observed wavelength of folds along the peripheral of the SPT, but all of these values either required an elevated thermal state or an amount of strain that has not presently been proven. Subsequent work will need to attempt to estimate the strain within the region to further constrain the thermal parameters.

G. References:

Barr, A.C., 2008. Mobile lid convection beneath Enceladus' south polar terrain. J. Geophys. Res. Planets 113, E07009. doi:10.1029/2008JE003114

Barr, A.C., Preuss, L.J., 2010. On the origin of south polar folds on Enceladus. Icarus 208, 499–503. doi:10.1016/j.icarus.2010.03.038

Beddingfield, C.B., Burr, D.M., Dunne, W.M., 2013. Evidence for Contraction Within the Leading Hemisphere Section of the South Polar Terrain Boundary, Enceladus. Presented at the Lunar and Planetary Science Conference, p. 1254.

Beeman, M., Durham, W.B., Kirby, S.H., 1988. Friction of ice. J. Geophys. Res. Solid Earth 93, 7625–7633. doi:10.1029/JB093iB07p07625

Bland, M.T., McKinnon, W.B., 2012. Forming Europa's folds: Strain requirements for the production of large-amplitude deformation. Icarus 221, 694–709. doi:10.1016/j.icarus.2012.08.029

Bland, M.T., McKinnon, W.B., Schenk, P.M., 2015. Constraining the heat flux between Enceladus' tiger stripes: Numerical modeling of funiscular plains formation. Icarus 260, 232–245. doi:10.1016/j.icarus.2015.07.016

Dombard, A.J., Cheng, A.F., 2008. Constraints on the Evolution of Iapetus from Simulations of Its Ridge and Bulge. Presented at the Lunar and Planetary Science Conference, p. 2262.

Dombard, A.J., McKinnon, W.B., 2006. Elastoviscoplastic relaxation of impact crater topography with application to Ganymede and Callisto. J. Geophys. Res. Planets 111, E01001. doi:10.1029/2005JE002445

Fink, J., 1980. Surface folding and viscosity of rhyolite flows. Geology 8, 250–254. doi:10.1130/0091-7613(1980)8<250:SFAVOR>2.0.CO;2

Fink, J.H., Fletcher, R.C., 1978. Ropy pahoehoe: Surface folding of a viscous fluid. J. Volcanol. Geotherm. Res. 4, 151–170. doi:10.1016/0377-0273(78)90034-3

Gammon, P.H., Kiefte, H., Clouter, M.J., 1983. Elastic constants of ice samples by Brillouin spectroscopy. J. Phys. Chem. 87, 4025–4029. doi:10.1021/j100244a004

Goguen, J.D., Buratti, B.J., Brown, R.H., Clark, R.N., Nicholson, P.D., Hedman, M.M., Howell, R.R., Sotin, C., Cruikshank, D.P., Baines, K.H., Lawrence, K.J., Spencer, J.R., Blackburn, D.G., 2013. The temperature and width of an active fissure on Enceladus measured with Cassini VIMS during the 14 April 2012 South Pole flyover. Icarus 226, 1128–1137. doi:10.1016/j.icarus.2013.07.012

Goldsby, D.L., Kohlstedt, D.L., 2001. Superplastic deformation of ice: Experimental observations. J. Geophys. Res. Solid Earth 106, 11017–11030. doi:10.1029/2000JB900336

Howett, C.J.A., Spencer, J.R., Pearl, J., Segura, M., 2011. High heat flow from Enceladus' south polar region measured using 10-600 cm-1 Cassini/CIRS data. J. Geophys. Res. Planets 116, E03003. doi:10.1029/2010JE003718

Hurford, T.A., Bills, B.G., Helfenstein, P., Greenberg, R., Hoppa, G.V., Hamilton, D.P., 2009. Geological implications of a physical libration on Enceladus. Icarus 203, 541–552. doi:10.1016/j.icarus.2009.04.025

Kieffer, S.W., Lu, X., Bethke, C.M., Spencer, J.R., Marshak, S., Navrotsky, A., 2006. A Clathrate Reservoir Hypothesis for Enceladus' South Polar Plume. Science 314, 1764–1766. doi:10.1126/science.1133519

Meyer, J., Wisdom, J., 2007. Tidal heating in Enceladus. Icarus 188, 535–539. doi:10.1016/j.icarus.2007.03.001

Nimmo, F., Spencer, J.R., Pappalardo, R.T., Mullen, M.E., 2007. Shear heating as the origin of the plumes and heat flux on Enceladus. Nature 447, 289–291. doi:10.1038/nature05783

Petrenko, V.F., Whitworth, R.W., 1999. Physics of Ice. OUP Oxford.

Porco, C.C., Helfenstein, P., Thomas, P.C., Ingersoll, A.P., Wisdom, J., West, R., Neukum, G., Denk, T., Wagner, R., Roatsch, T., Kieffer, S., Turtle, E., McEwen, A., Johnson, T.V., Rathbun, J., Veverka, J., Wilson, D., Perry, J., Spitale, J., Brahic, A., Burns, J.A., DelGenio, A.D., Dones, L., Murray, C.D., Squyres, S., 2006. Cassini Observes the Active South Pole of Enceladus. Science 311, 1393–1401. doi:10.1126/science.1123013

Roberts, J.H., Nimmo, F., 2008. Near-surface heating on Enceladus and the south polar thermal anomaly. Geophys. Res. Lett. 35, L09201. doi:10.1029/2008GL033725

Spencer, J.R., Pearl, J.C., Segura, M., Flasar, F.M., Mamoutkine, A., Romani, P., Buratti, B.J., Hendrix, A.R., Spilker, L.J., Lopes, R.M.C., 2006. Cassini Encounters Enceladus: Background and the Discovery of a South Polar Hot Spot. Science 311, 1401–1405. doi:10.1126/science.1121661

White, O.L., Schenk, P.M., Dombard, A.J., 2013. Impact basin relaxation on Rhea and Iapetus and relation to past heat flow. Icarus 223, 699–709. doi:10.1016/j.icarus.2013.01.013

V. APPENDICES

A. Appendix A. MARC Iapetus thermal file and mechanical .dat File

The MARC finite element package has been used extensively for simulating lithospheric deformation. For our models, we do a steady state thermal simulation (shown first) followed up a mechanical simulation. We input these files into the MARC finite element package to build a complete simulation: a .dat file for the thermal simulation, a .dat file for the mechanical simulation, and a user-subroutine file (or .f file, in Appendix B). These are abridged .dat files that do not include the element and geometry of the meshes. In various sections, I annotate certain items (lines that start with $ are not read by the MARC package). Readers are encouraged to refer to the MARC user manuals for a complete set of explanation.

The .dat file has three main sections: 1) The Parameter section, which determines the general structure that the simulation will be implementing; 2) The Model Definition section, which determines the geometric and physical conditions under which the simulation will be operating; and 3) The History Definition section, which determines the time-stepping aspects of the simulation.

$Start of thermal .dat file

```
sizing                  0    5000    5151    101
alloc              25
elements              40
```

$ These lines create the framework for the number of elements in the mesh and the element type used in the mesh. Element type 40 refers to an axisymmetric quadrilateral thermal element.

```
version             11
table              0    0    2    1    1    0    0    1
processor            1    1    1    0
$no list
heat               0    0    1    0    1    1
all points
no echo             1    2    3
setname             29
end
$..................
connectivity
     0     0     1
     1    39     1     5    83    64
     2    39    64    83    84    65
   999    39  1041  1070  1071  1042
  1000    39  1042  1071     3    42
coordinates
     3  1071     0     1
     1 4.000000000000000+3-9.999999999964793-1 0.000000000000000+0
     2 0.000000000000000+0 1.000000000000000+0 0.000000000000000+0
  1070 0.000000000000000+0-7.228444444444446+3 0.000000000000000+0
  1071 0.000000000000000+0-7.608777777777778+3 0.000000000000000+0

isotropic

      1    0    0    0    0material1
 1.000000000000000+0 1.000000000000000+3 9.500000000000000+2 0.000000000000000+0
0.000000000000000+0 0.000000000000000+0 0.000000000000000+0
      2    0    0    0    0    0    0
       1     to    5000
```

$ These are the parameters for establishing the thermal conductivity, capacity and density. For ice, we use a temperature dependent thermal conductivity that is defined in Table 2.

```
table          table1
      1    1    0    0    3
      6  101    2    0    0    2    0    0    2    0    0    2
60+30*sin(asin((v1/1115000)))^.25
table          table2
      1    1    0    0    3
     12   11    2    0    0    2    0    0    2    0    0    2
```

651/(v1+0.0000001)
$The above two sections establish the use of equations to govern different nodal vales for surface temperature and thermal conductivity respectively.
geometry

```
 0.000000000000000+0 0.000000000000000+0 0.000000000000000+0 1.000000000000000+0
0.000000000000000+0 0.000000000000000+0 0.000000000000000+0
          1         to        5000
```

initial temp

```
         1         0         0         0         0         0icond1
 7.000000000000000+1
         0
         2
icond1_nodes
```

$established an initial temperature of the mesh

fixed temperature

```
         1         0         0         0         0         0surface
 1.000000000000000+0
         1
         1
         2
surface_nodes
```

$ This calls the Table 1 from above to tell it what temperature to be at each node
dist fluxes

```
         1         0         0         0         0         0bottom
 5.000000000000000-4
         0
         0        10
        13
bottom_edges
```

$This is the heat flow in W m^{-2} of the mesh

```
         1         0         0         0         0         0sides
 0.000000000000000+0
         0
         0        10
        13
sides_edges
```

$Zero heat can leak through the sides of the mesh

```
loadcase           job1
         4
icond1
bottom
```

```
sides
surface
no print
post
       0      16      17       0       0      19      20       0       1       0       0       0       0
0       0       0
parameters
 1.000000000000000+0 1.000000000000000+9 1.000000000000000+2 1.000000000000000+6
2.500000000000000-1 5.000000000000000-1 1.500000000000000+0-5.000000000000000-1
 8.625000000000000+0 2.000000000000000+1 1.000000000000000-4 1.000000000000000-6
1.000000000000000+0 1.000000000000000-4
 8.314000000000000+0 2.731500000000000+2 5.000000000000000-1 0.000000000000000+0
5.670510000000000-8 1.438769000000000-2 2.997900000000000+8 1.00000000000000+30
 0.000000000000000+0 0.000000000000000+0 1.000000000000000+2 0.000000000000000+0
1.000000000000000+0-2.000000000000000+0 1.000000000000000+6
 0.000000000000000+0 0.000000000000000+0 1.256637061000000-6 8.85418781700000-12
1.200000000000000+2
end option
$..................
$....start of loadcase lcase1
title           lcase1
loadcase            lcase1
       3
bottom
sides
surface
control
    99999      10       0       0       0       0       0       0       1       0       0       0
 2.000000000000000+1 1.000000000000000+2 0.000000000000000+0 1.000000000000000+2
1.000000000000000-1 1.000000000000000-1 1.000000000000000-1 1.00000000000000+30
parameters
 1.000000000000000+0 1.000000000000000+9 1.000000000000000+2 1.000000000000000+6
2.500000000000000-1 5.000000000000000-1 1.500000000000000+0-5.000000000000000-1
 8.625000000000000+0 2.000000000000000+1 1.000000000000000-4 1.000000000000000-6
1.000000000000000+0 1.000000000000000-4
 8.314000000000000+0 2.731500000000000+2 5.000000000000000-1 0.000000000000000+0
5.670510000000000-8 1.438769000000000-2 2.997900000000000+8 1.00000000000000+30
 0.000000000000000+0 0.000000000000000+0 1.000000000000000+2 0.000000000000000+0
1.000000000000000+0-1.000000000000000+0 1.000000000000000+6
 0.000000000000000+0 0.000000000000000+0 1.256637061000000-6 8.85418781700000-12
1.200000000000000+2
time step
 0.000000000000000+0
steady state
continue
$....end of loadcase lcase1
```

```
$..................
$Zero time steps iterate the thermal solution and are done 10 times to establish a state solution.

$Start of Mechanical .dat file
sizing                    0     5000     5151      254
alloc             25
elements            10
$ These lines create the framework for the number of elements in the mesh and the element type
used in the mesh. Element type 10 refers to an axisymmetric quadrilateral mechanical element.
version           11
table             0       0       2       1       1       0       0       1
processor          1       1       1       0
$no list
large stra         1       0
$Allows for the use of large strain formulation
follow for         1       0       0
creep             0       0       0       0
constant
assumed
all points
istress
$Adds the overburden to the model
no echo            1       2       3
setname            27
end
$..................
1lin mohrc        isotropic               0       0       0       0material1
 9.332000000000003+9 3.252000000000000-1 9.500000000000000+2 0.000000000000000+0
1.462000000000000+6 1.550000000000000-1 0.000000000000000+0 0.000000000000000+0
         0       0       0       0       0       0       0       0
          1        to       5000
creep           data
         0       0       0       0 0.000000000000000000000000+0
0.000000000000000000000000+0 0.000000000000000000000000+0        0       1       0
         0       0       0       0       0
$ The previous sections allow various inputs of elastic and plastic material properties and mass
density through the Mohr-Coulomb criteria. The creep section calls the CRPLAW subroutine (in
the .f file)

geometry

 0.000000000000000+0 1.000000000000000+0 0.000000000000000+0 1.000000000000000+0
0.000000000000000+0 0.000000000000000+0 0.000000000000000+0
          1        to       5000
init stress
```

```
        1         1         0         0         0         0istress
 0.000000000000000+0 1.000000000000000+0 0.000000000000000+0 1.000000000000000+0
0.000000000000000+0 0.000000000000000+0 0.000000000000000+0
        0         0         0         0         0         0
        1
istress_elements
fixed disp

        1         0         0         0         1         0bottom
 0.000000000000000+0
        0
        1
        2
bottom_nodes
        1         0         0         0         1         0bside
 0.000000000000000+0
        0
        2
        2
bside_nodes
        1         0         0         0         1         0itside
 0.000000000000000+0
        0
        2
        2
itside_nodes
$ Bottom, bside, and itside each act as a free slip surface
        1         0         0         0         1         0tside
-1.115000000000000+5
        0
        2
        2
tside_nodes
$This boundary condition acts as the fixed displacement and drives the 10% shortening of the
lithosphere
dist loads

        1         0         0         0         0         0grav
-2.230000000000000-1 0.000000000000000+0
        0         0
        0       102
        1
grav_elements
$This applys gravity to the mesh
initial temp
```

```
        1         2         0        10         0       0thermal
$This incorporates the thermal state from the solution to the thermal .dat file.
loadcase           job1
        6
bottom
bside
itside
thermal
istress
grav
no print
udump

post
        6       16       17        0        0       19       20        0    11111        0        0        0        0
0        0        0
        9        0
       17        0
      127        0
      311        0
       -1        0diff
       -2        0vis
parameters
 1.000000000000000+0 1.000000000000000+9 1.000000000000000+2 1.000000000000000+6
2.500000000000000-1 5.000000000000000-1 1.500000000000000+0-5.000000000000000-1
 8.625000000000000+0 2.000000000000000+1 1.000000000000000-4 1.000000000000000-6
1.000000000000000+0 1.000000000000000-4
 8.314000000000000+0 2.731500000000000+2 5.000000000000000-1 0.000000000000000+0
5.670510000000000-8 1.438769000000000-2 2.997900000000000+8 1.00000000000000+30
 0.000000000000000+0 0.000000000000000+0 1.000000000000000+2 0.000000000000000+0
1.000000000000000+0-2.000000000000000+0 1.000000000000000+6
 0.000000000000000+0 0.000000000000000+0 1.256637061000000-6 8.854187817000000-12
1.200000000000000+2
end option
$..................
$....start of loadcase lcase1
title              lcase1
loadcase           lcase1
        4
bottom
bside
itside
grav
control
    99999       10        0        0        0        1        0        0        1        0        1        0
```

```
 1.000000000000000-1 0.000000000000000+0 0.000000000000000+0 0.000000000000000+0
0.000000000000000+0 0.000000000000000+0 0.000000000000000+0 0.000000000000000+0
parameters
 1.000000000000000+0 1.000000000000000+9 1.000000000000000+2 1.000000000000000+6
2.500000000000000-1 5.000000000000000-1 1.500000000000000+0-5.000000000000000-1
 8.625000000000000+0 2.000000000000000+1 1.000000000000000-4 1.000000000000000-6
1.000000000000000+0 1.000000000000000-4
 8.314000000000000+0 2.731500000000000+2 5.000000000000000-1 0.000000000000000+0
5.670510000000000-8 1.438769000000000-2 2.997900000000000+8 1.00000000000000+30
 0.000000000000000+0 0.000000000000000+0 1.000000000000000+2 0.000000000000000+0
1.000000000000000+0-1.000000000000000+0 1.000000000000000+6
 0.000000000000000+0 0.000000000000000+0 1.256637061000000-6 8.85418781700000-12
1.200000000000000+2
creep increment
 0.000000000000000000000000+0
continue
$....end of loadcase lcase1
$ The zero time increment iterate the elastic solution and is repeated 10 times.
$....start of loadcase lcase2
title            lcase2
loadcase           lcase2
        4
bottom
bside
tside                                                               2
grav
control
    99999     9990        0        0        0        1        0        0        1        0        1        0
 1.000000000000000-1 0.000000000000000+0 0.000000000000000+0 0.000000000000000+0
0.000000000000000+0 0.000000000000000+0 0.000000000000000+0 0.000000000000000+0
parameters
 1.000000000000000+0 1.000000000000000+9 1.000000000000000+2 1.000000000000000+6
2.500000000000000-1 5.000000000000000-1 1.500000000000000+0-5.000000000000000-1
 8.625000000000000+0 2.000000000000000+1 1.000000000000000-4 1.000000000000000-6
1.000000000000000+0 1.000000000000000-4
 8.314000000000000+0 2.731500000000000+2 5.000000000000000-1 0.000000000000000+0
5.670510000000000-8 1.438769000000000-2 2.997900000000000+8 1.00000000000000+30
 0.000000000000000+0 0.000000000000000+0 1.000000000000000+2 0.000000000000000+0
1.000000000000000+0-1.000000000000000+0 1.000000000000000+6
 0.000000000000000+0 0.000000000000000+0 1.256637061000000-6 8.85418781700000-12
1.200000000000000+2
auto creep
 1.000000000000000000000000+0 3.155000000000000000000000+15   9999999       40
90        0 0.000000000000000+0
 5.000000000000000-2 5.000000000000000+2 5.000000000000000-2        0        0
continue
```

$....end of loadcase lcase2
$..................
$ *auto creep* defines the details of the simulation time.

B. Appendix B. Iapetus folding .f File

The following is a subroutine file that is written in FORTRAN and completes the model when added to the .dat file. Readers are encouraged to read Volume D of the MARC manual for further information. Lines starting with *C* are not read by the system.

These have all been adapted from previous work by Dr. Andrew Dombard.

C The *CPRLAW* subroutine determines the strain rate by calculating various C creep values.

```
C
      SUBROUTINE
CRPLAW(EQCP,EQCPNC,STR,CRPE,T,DT,TIMINC,CPTIM,M,NN,KC,
     *          MATS,NDI,NSHEAR)
C
      IMPLICIT REAL*8 (A-H,O-Z)
C
      DIMENSION T(3),DT(1),STR(1),CRPE(1)
C
    GS = 1.d-3
      RT = 8.31451d0*DT(1)
    dis = (4.d5)*((T(1)/1.0d+6)**(4.d0))*dexp(-60.d3/RT)
      dif = (3.02d-8)*(T(1)/(DT(1)*GS*GS))*(dexp(-59.4d3/RT) +
     *          2.84d-9*dexp(-60.d3/RT)/GS)
      GBS = ((3.9d-3)/(GS**1.4d0))*((T(1)/1.0d+6)**(1.8d0))*
     *          dexp(-49.d3/RT)
      ES = (5.5d+7)*((T(1)/1.0d+6)**(2.4d0))*dexp(-60.d3/RT)
C
      rate = 1.d0/(1.d0/GBS + 1.d0/ES) + dis + dif
      viscmin = 1.d21
C     if (cptim.gt.3.15576d12) viscmin = 1.d18
C     if (cptim.gt.6.31152d12) viscmin = 1.d19
      eta = T(1)/(3.d0*rate)
      if (eta.lt.viscmin) rate = T(1)/(3.d0*viscmin)
      EQCPNC = TIMINC*rate
C
      RETURN
      END
C
C-----------------------------------------------------------------------------
C
C This subroutine is used to calculate the initial stress of the system
```

```
      SUBROUTINE
UINSTR(S,NDI,NSHEAR,Nl,NNl,KCl,XINTP,NCRDl,INC,TIME,TIMEINC)
C
      IMPLICIT REAL*8 (A-H,O-Z)
C
      DIMENSION S(1),XINTP(NCRD),Nl(2)
      DIMENSION CCNODE(12)
C
      parameter(GP = 0.577350269189626d0)
C
      include '/opt/msc/marc2010.2/common/lass'
      include '/opt/msc/marc2010.2/common/dimen'
      include '/opt/msc/marc2010.2/common/space'
      include '/opt/msc/marc2010.2/common/blnk'
      include '/opt/msc/marc2010.2/common/array2'
      include '/opt/msc/marc2010.2/common/spacevec'
      include '/opt/msc/marc2010.2/common/strvar'
C
      if (nnl.eq.1) then
        eta1 = -1.d0*GP
        eta2 = -1.d0*GP
      endif
      if (nnl.eq.2) then
        eta1 = 1.d0*GP
        eta2 = -1.d0*GP
      endif
      if (nnl.eq.3) then
        eta1 = -1.d0*GP
        eta2 = 1.d0*GP
      endif
      if (nnl.eq.4) then
        eta1 = 1.d0*GP
        eta2 = 1.d0*GP
      endif
C     Quadralateral Elements
      x = 0.d0
      y = 0.d0
      JRDPRE = 0
C     CALL VECFTC(CCNODE,VARS(IXORD),NCRDMX,NCRD,lm(1),JRDPRE,2,1)
      CALL VECFTC(CCNODE,XORD_D,NCRDMX,NCRD,lm(1),JRDPRE,2,1)
      x = x + (1.d0 - eta1)*(1.d0 - eta2)*ccnode(1)/4.d0
      y = y + (1.d0 - eta1)*(1.d0 - eta2)*ccnode(2)/4.d0
      JRDPRE = 0
C     CALL VECFTC(CCNODE,VARS(IXORD),NCRDMX,NCRD,lm(2),JRDPRE,2,1)
      CALL VECFTC(CCNODE,XORD_D,NCRDMX,NCRD,lm(2),JRDPRE,2,1)
      x = x + (1.d0 + eta1)*(1.d0 - eta2)*ccnode(1)/4.d0
```

```
      y = y + (1.d0 + eta1)*(1.d0 - eta2)*ccnode(2)/4.d0
      JRDPRE = 0
C     CALL VECFTC(CCNODE,VARS(IXORD),NCRDMX,NCRD,lm(3),JRDPRE,2,1)
      CALL VECFTC(CCNODE,XORD_D,NCRDMX,NCRD,lm(3),JRDPRE,2,1)
      x = x + (1.d0 + eta1)*(1.d0 + eta2)*ccnode(1)/4.d0
      y = y + (1.d0 + eta1)*(1.d0 + eta2)*ccnode(2)/4.d0
      JRDPRE = 0
C     CALL VECFTC(CCNODE,VARS(IXORD),NCRDMX,NCRD,lm(4),JRDPRE,2,1)
      CALL VECFTC(CCNODE,XORD_D,NCRDMX,NCRD,lm(4),JRDPRE,2,1)
      x = x + (1.d0 - eta1)*(1.d0 + eta2)*ccnode(1)/4.d0
      y = y + (1.d0 - eta1)*(1.d0 + eta2)*ccnode(2)/4.d0
C
C  Stress Profile Parameters:
      rho =  950.d0
      g = 0.223d0
C
      S(1) = rho*g*x
      S(2) = rho*g*x
      S(3) = rho*g*x
C
      RETURN
      END
C
C-----------------------------------------------------------------------------
```

C The *IMPD* subroutine builds a record of displacements at select nodes at the end of each increment. This subroutine is working in conjunction with the UDUMP option in the Model Definition.

```
C

      subroutine impd(n,dd,td,xord,f,v,a,nd,ncrd)
C
      IMPLICIT REAL*8 (A-H,O-Z)
C
      dimension dd(nd),td(nd),xord(ncrd),f(nd),v(nd),a(nd),n(2)
C
      include '/opt/msc/marc2010.2/common/creeps'
      include '/opt/msc/marc2010.2/common/concom'

      open(10,file='youngs.txt',status='unknown')
C
      if (n(1).eq.1) d1 = td(1)
      if (n(1).eq.2) write(10,666)inc,cptim/3.15576d7,td(1) - d1
666   format(i6,e13.5,f9.2)
C
      return
```

```
      end
C
C---------------------------------------------------------------------------
C This subroutine allows the user to define an element variable to be written to C the post file.

C

      subroutine plotv(v,s,sp,etot,eplas,ecreep,t,m,nn,layer,ndi,
   *  nshear,jpltcd)
C     SUBROUTINE PLOTV(V,S,SP,ETOT,EPLAS,ECREEP,T,M,NN,LAYER,NDI,
C    *         NSHEAR,JPLNCD)
C
C     include '/opt/msc/marc2010.2/common/implicit'
      IMPLICIT REAL*8 (A-H,O-Z)
      dimension s(*),etot(*),eplas(*),ecreep(*),sp(*),m(2)
C     DIMENSION S(1),SP(1),ETOT(1),EPLAS(1),ECREEP(1),M(2)
C
      if (jpltcd.lt.2) then
       V = S(1) - S(2)
      else
       smean = (s(1) + s(2) + s(3))/3.d0
       s1 = s(1) - smean
       s2 = s(2) - smean
       s3 = s(3) - smean
       es = dsqrt((s1*s1 + s2*s2 + s3*s3)/2.d0 + s(4)*s(4))
     GS = 1.d-3
       RT = 8.31451d0*T
     dis = (4.d5)*((es/1.0d+6)**(4.d0))*dexp(-60.d3/RT)
       dif = (3.02d-8)*(es/(T*GS*GS))*(dexp(-59.4d3/RT) +
   *         2.84d-9*dexp(-60.d3/RT)/GS)
       GBS = ((3.9d-3)/(GS**1.4d0))*((es/1.0d+6)**(1.8d0))*
   *         dexp(-49.d3/RT)
       ESS = (5.5d+7)*((es/1.0d+6)**(2.4d0))*dexp(-60.d3/RT)
       r = 1.d0/(1.d0/GBS + 1.d0/ESS) + dis + dif
       V = dlog10(dabs(es)) - dlog10(dabs(3.d0*r))
      endif
C
      RETURN
      END
C
C=========================================================================
=======
C The following was used only in certain Enceladus simulations as a test to determine the effect of strain weakening on the simulations. In the future, it will be incorporated into all simulations done in icy rheologies.
C---------------------------------------------------------------------------
```

```
C
      SUBROUTINE WKSLP(M,NN,KCUS,MATUS,SLOPE,EBARP,ERAT,STRYT,DT,
   *  IFIRST)
      IMPLICIT REAL *8 (A-H, O-Z)
      DIMENSION MATUS(2),KCUS(2)
      A= 8.d-1
      eref = 3.d0
      c0 = 1.d6
      STRYT = 1.462d0*c0*(1.d0-0.866d0*A*(EBARP/eref))
      SLOPE = -(1.462d0*A*c0)/eref
C
      RETURN
      END
C
C===================================================================
========
```

C. Appendix C. Mercury .f File

The following is a subroutine file that is written in FORTRAN and completes the model when added to the .dat file. It is similar to the previously discussed .f file that was used for Iapetus, however there are changes to the CRPLAW and UINSTR subroutines that govern the differences in creep in rock and 2 layer models in stress.

These have all been adapted from previous work by Dr. Andrew Dombard.

```
C
      SUBROUTINE
CRPLAW(EQCP,EQCPNC,STR,CRPE,T,DT,TIMINC,CPTIM,M,NN,KC,
   *           MATS,NDI,NSHEAR)
C
      IMPLICIT REAL*8 (A-H,O-Z)
C
      DIMENSION T(3),DT(1),STR(1),CRPE(1)
C
      if (MATS.eq.1) then
C*******Mackwell et al. [1998] - dry Maryland diabase
        creep = (8.d0)*((T(1)/1.0d+6)**(4.7d0))*
   *          dexp(-485.d3/(8.31451d0*DT(1)))
      else
C*******Karato and Wu [1993] - dry
        dis = (3.5d+22)*((T(1)/80.d+9)**(3.5d0))*
   *          dexp(-540.d3/(8.31451d0*DT(1)))
        dif = (8.7d+15)*(T(1)/80.d+9)*((0.5d-9/1.d-3)**(2.5))*
   *          dexp(-300.d3/(8.31451d0*DT(1)))
        creep = dis + dif
      endif
C
      etamin = 1.d23
C     if (cptim.gt.6.31152d12) viscmin = 1.d19
      eta = T(1)/(3.d0*creep)
      if (eta.lt.etamin) creep = T(1)/(3.d0*etamin)
      EQCPNC = TIMINC*creep
C
      RETURN
      END
C
C---------------------------------------------------------------------------
C
      SUBROUTINE
UINSTR(S,NDI,NSHEAR,Nl,NNl,KCl,XINTP,NCRDl,INC,TIME,TIMEINC)
```

```
C
      IMPLICIT REAL*8 (A-H,O-Z)
C
      DIMENSION S(1),XINTP(NCRD),Nl(2)
      DIMENSION CCNODE(12)
C
      parameter(GP = 0.577350269189626d0)
C
      include '/opt/msc/marc2010.2/common/lass'
      include '/opt/msc/marc2010.2/common/dimen'
      include '/opt/msc/marc2010.2/common/space'
      include '/opt/msc/marc2010.2/common/blnk'
      include '/opt/msc/marc2010.2/common/array2'
      include '/opt/msc/marc2010.2/common/spacevec'
      include '/opt/msc/marc2010.2/common/strvar'
C
      if (nnl.eq.1) then
        eta1 = -1.d0*GP
        eta2 = -1.d0*GP
      endif
      if (nnl.eq.2) then
        eta1 = 1.d0*GP
        eta2 = -1.d0*GP
      endif
      if (nnl.eq.3) then
        eta1 = -1.d0*GP
        eta2 = 1.d0*GP
      endif
      if (nnl.eq.4) then
        eta1 = 1.d0*GP
        eta2 = 1.d0*GP
      endif
C     Quadralateral Elements
      x = 0.d0
      y = 0.d0
      JRDPRE = 0
C     CALL VECFTC(CCNODE,VARS(IXORD),NCRDMX,NCRD,lm(1),JRDPRE,2,1)
      CALL VECFTC(CCNODE,XORD_D,NCRDMX,NCRD,lm(1),JRDPRE,2,1)
      x = x + (1.d0 - eta1)*(1.d0 - eta2)*ccnode(1)/4.d0
      y = y + (1.d0 - eta1)*(1.d0 - eta2)*ccnode(2)/4.d0
      JRDPRE = 0
C     CALL VECFTC(CCNODE,VARS(IXORD),NCRDMX,NCRD,lm(2),JRDPRE,2,1)
      CALL VECFTC(CCNODE,XORD_D,NCRDMX,NCRD,lm(2),JRDPRE,2,1)
      x = x + (1.d0 + eta1)*(1.d0 - eta2)*ccnode(1)/4.d0
      y = y + (1.d0 + eta1)*(1.d0 - eta2)*ccnode(2)/4.d0
      JRDPRE = 0
```

```
C       CALL VECFTC(CCNODE,VARS(IXORD),NCRDMX,NCRD,lm(3),JRDPRE,2,1)
        CALL VECFTC(CCNODE,XORD_D,NCRDMX,NCRD,lm(3),JRDPRE,2,1)
        x = x + (1.d0 + eta1)*(1.d0 + eta2)*ccnode(1)/4.d0
        y = y + (1.d0 + eta1)*(1.d0 + eta2)*ccnode(2)/4.d0
        JRDPRE = 0
C       CALL VECFTC(CCNODE,VARS(IXORD),NCRDMX,NCRD,lm(4),JRDPRE,2,1)
        CALL VECFTC(CCNODE,XORD_D,NCRDMX,NCRD,lm(4),JRDPRE,2,1)
        x = x + (1.d0 - eta1)*(1.d0 + eta2)*ccnode(1)/4.d0
        y = y + (1.d0 - eta1)*(1.d0 + eta2)*ccnode(2)/4.d0
C
C  Stress Profile Parameters:
        rhoc = 2900.d0
        rhom = 3200.d0
        g = 3.70d0
C
        if(x.ge.-100.d3) then
          S(1) = rhoc*g* x
          S(2) = rhoc*g* x
          S(3) = rhoc*g* x
        else
          S(1) = rhom*g*(x + 100.d3) - rhoc*g*100.d3
          S(2) = rhom*g*(x + 100.d3) - rhoc*g*100.d3
          S(3) = rhom*g*(x + 100.d3) - rhoc*g*100.d3
        endif
C
        RETURN
        END
C
C-----------------------------------------------------------------------------
C
        subroutine plotv(v,s,sp,etot,eplas,ecreep,t,m,nn,layer,ndi,
     *  nshear,jpltcd)
C       SUBROUTINE PLOTV(V,S,SP,ETOT,EPLAS,ECREEP,T,M,NN,LAYER,NDI,
C    *            NSHEAR,JPLNCD)
C
C       include '/opt/msc/marc2010.2/common/implicit'
        IMPLICIT REAL*8 (A-H,O-Z)
        dimension s(*),etot(*),eplas(*),ecreep(*),sp(*),m(2)
C       DIMENSION S(1),SP(1),ETOT(1),EPLAS(1),ECREEP(1),M(2)
C
        if (jpltcd.lt.2) then
          V = S(1) - S(2)
        else
          smean = (s(1) + s(2) + s(3))/3.d0
          s1 = s(1) - smean
          s2 = s(2) - smean
```

```
          s3 = s(3) - smean
          es = dsqrt((s1*s1 + s2*s2 + s3*s3)/2.d0 + s(4)*s(4))
        GS = 1.d-3
          RT = 8.31451d0*T
          if (M(1).le.500) then
C*******Mackwell et al. [1998] - dry Maryland diabase
           r = (8.d0)*((es/1.0d+6)**(4.7d0))*
    *            dexp(-485.d3/RT)
          else
C*******Karato and Wu [1993] - dry
           dis = (3.5d+22)*((es/80.d+9)**(3.5d0))*
    *            dexp(-540.d3/RT)
           dif = (8.7d+15)*(es/80.d+9)*((0.5d-9/GS)**(2.5))*
    *            dexp(-300.d3/RT)
           r = dis + dif
          endif
          V = dlog10(dabs(es)) - dlog10(dabs(3.d0*r))
        endif
C
        RETURN
        END
C
C===================================================================
=====
```

D. Appendix D. Python file used for generating txt file from Mercury/Enceladus data

The following is a python script used for rapidly generating different path plots for export that was used for processing the Mercury and Enceladus data.

```
from py_mentat import *

def main ():
    py_send("*post_close")
    py_send("*post_open l14_m.t16")
    py_send("*fill_view")
    py_send("*set_deformed both")
    py_send("*post_contour_bands")
    py_send("*post_skip_to_last")
    py_send("*post_prev")
    py_send("*set_pathplot_path")
    py_send("1 2 #")
    py_send("*pathplot_add")
    py_send("Arc Length")
    py_send("Displacement X")
    py_send("*show_pathplot")
    py_send("*pathplot_fit")
    py_send("*fill_view")
    py_send("*pathplot_fit")
    py_send("*get_path_plots")
    py_send("*xy_plot_fit")
    py_send("*pathplot_fit")
    py_send("*get_path_plots")
    py_send("*post_next")
    py_send("*get_path_plots")
    py_send("*xy_plot_fit")
    py_send("*xy_plot_export l6.txt")
    py_send("y")
    py_send("*xy_plot_clear")
```

E. Appendix E. Raw data for Chapter III

Table 1. Summary of model results for full-compensated topography

	6 mW m^{-2}			25 mW m^{-2}			40 mW m^{-2}		
	1 km	2 km	3 km	1 km	2 km	3 km	1 km	2 km	3 km
l6	0.952	0.928	0.916	0.937	0.933	0.928	0.929	0.925	0.920
l8	0.969	0.981	0.990	0.930	0.921	0.913	0.918	0.909	0.900
l10	1.012	1.019	1.023	0.964	0.950	0.935	0.946	0.932	0.917
l12	1.014	1.020	1.024	0.953	0.934	0.913	0.928	0.909	0.887
l14	1.013	1.017	1.021	0.942	0.918	0.890	0.907	0.883	0.854
l16	1.010	1.014	1.017	0.931	0.902	0.867	0.884	0.855	0.819
l18	1.008	1.011	1.013	0.921	0.889	0.851	0.862	0.827	0.786
l20	1.006	1.009	1.011	0.917	0.882	0.841	0.841	0.800	0.753
l22	1.005	1.007	1.009	0.911	0.874	0.833	0.819	0.775	0.726
l24	1.004	1.005	1.007	0.914	0.876	0.837	0.805	0.756	0.704

Table 2. Summary of model results for uncompensated topography

	6 mW m^{-2}			25 mW m^{-2}			40 mW m^{-2}		
	1 km	2 km	3 km	1 km	2 km	3 km	1 km	2 km	3 km
l6	0.713	0.552	0.453	0.095	0.094	0.094	0.092	0.091	0.091
l8	0.714	0.638	0.600	0.100	0.097	0.096	0.091	0.090	0.089
l10	0.838	0.802	0.779	0.111	0.104	0.101	0.092	0.089	0.088
l12	0.915	0.895	0.881	0.132	0.119	0.113	0.094	0.090	0.088
l14	0.954	0.942	0.933	0.165	0.143	0.133	0.101	0.093	0.090
l16	0.974	0.966	0.961	0.212	0.179	0.163	0.115	0.103	0.097
l18	0.985	0.980	0.977	0.272	0.228	0.205	0.130	0.112	0.105
l20	0.991	0.988	0.986	0.344	0.289	0.258	0.155	0.130	0.119
l22	0.994	0.992	0.991	0.421	0.358	0.321	0.187	0.154	0.139
l24	0.997	0.995	0.995	0.500	0.431	0.390	0.228	0.186	0.166

Table 3. Summary of model results for uniform crustal thickness

	6 mW m^{-2}			25 mW m^{-2}			40 mW m^{-2}		
	1 km	2 km	3 km	1 km	2 km	3 km	1 km	2 km	3 km
l6	0.683	0.505	0.395	0.000	0.001	0.001	0.003	0.003	0.003
l8	0.684	0.599	0.557	0.006	0.003	0.002	0.002	0.003	0.004
l10	0.820	0.781	0.755	0.020	0.013	0.010	0.000	0.002	0.003
l12	0.906	0.883	0.867	0.044	0.031	0.024	0.005	0.001	0.000
l14	0.949	0.935	0.926	0.082	0.059	0.048	0.015	0.008	0.005
l16	0.966	0.956	0.950	0.143	0.108	0.090	0.030	0.018	0.013
l18	0.983	0.977	0.974	0.203	0.156	0.131	0.052	0.034	0.027
l20	0.990	0.986	0.984	0.283	0.224	0.192	0.082	0.057	0.046
l22	0.993	0.991	0.990	0.370	0.302	0.263	0.121	0.087	0.072
l24	1.003	1.004	1.004	0.457	0.384	0.340	0.168	0.125	0.105

Jonathan P. Kay

VI. Curriculum Vitae

University of Illinois at Chicago
Department of Earth and Environmental Science
845 West Taylor Street (MC 186)
Chicago, Illinois 60607-7059

Phone: 917-626-1933
Email: jkay5@uic.edu

EDUCATION

2017	Ph.D. Earth and Environmental Science, UIC, Chicago, IL Advisor: Dr. Andrew Dombard
2010	M.S., Department of Geology, University of Idaho, Moscow, ID Advisor: Dr. Simon A. Kattenhorn
2008	B.A. *with honors*, Department of Physics, Wheaton College, Norton, MA Advisors: Dr. John Collins and Dr. Geoff Collins

RESEARCH EXPERIENCE

2010-2016	Ph.D. Thesis Project, Title: "Unstable folding of lithospheres: Constraining the thermal history of a planetary body" University of Illinois at Chicago, Chicago, IL
2015	Internship (Pioneer Natural Resources) What is the present geothermal maturity of the Delaware Basin within the Permian Basin?
2008-2010	Masters Thesis Project, Title: "Is there evidence for recent tectonic activity on Jupiter's moon Europa?" University of Idaho, Moscow, ID
2007-2008	Undergraduate Thesis Title: "Estimating runoff rates on Titan from rainfall models" Wheaton College, Norton, MA Supervisor: Dr. Geoff Collins, Wheaton College
2007	Research Assistant, United States Geologic Survey Astrogeology, Flagstaff, AZ Supervisor: Dr. Ken Tanaka, Northern Arizona University
2006-2007	Research Assistant, Ganymede Global Mapping Project, Crater mapping and Counting, Wheaton College, Norton, MA Supervisor: Dr. Geoff Collins, Wheaton College (MA), and Dr. Wesley Patterson, APL.

PROFESSIONAL PUBLICATIONS

J. Kay, A. J. Dombard, Formation of the equatorial bulge on Iapetus through folding (In prep.)

J. Kay, A.J. Dombard, Contractually induced folding unlikely to induce folding on Mercury (In prep.)

J. Kay, A. J. Dombard, Simulating spatial variations of lithospheric folding in the South Polar Terrain of Enceladus (In prep.)

G. Collins, G. W. Patterson, J. Head, R. Pappalardo, L. Prockter, B. Lucchitta, and **J. Kay**, Global geologic map of Ganymede, United States Geological Survey Science Investigations Map Series #3237, 2013.

Dombard, A.J., A.F. Cheng, W.B. McKinnon, and **J.P. Kay**, Delayed Formation of the Equatorial Ridge on Iapetus from a Sub-Satellite Created in a Giant Impact, Journal of Geophysical Research, vol. 117, E03002, doi:10.1029/2011JE004010, 2012.

PRESENTATIONS AT SCIENTIFIC CONFERENCES

Kay, J.P., Dombard, A.J., 2017. Simulating Spatial Variations of Lithospheric Folding in the South Polar Terrain of Enceladus. Lunar Planet. Sci. XLVIII. Abstract 2580.

Kay, J.P., Dombard, A.J., 2017. A Test for Developing Long-Wavelength Lithospheric Folding on Mercury. Lunar Planet. Sci. XLVIII. Abstract 1657.

Kay, J.P., Dombard, A.J., 2014. An alternative explanation for the formation of the equatorial bulge of Iapetus. Rocky Mountain Rendezvous Laramie, WY

Kay, J.P., Dombard, A.J., 2013. How does contraction influence the formation of the equatorial bulge of Iapetus? American Association Petroleum Geologists Spring Break Conference Norman, OK

Kay, J.P., Dombard, A.J., 2012. Can unstable deformation form the equatorial bulge of Iapetus? American Association Petroleum Geologists Student Conference Morgantown, WV

Kay, J.P., Dombard, A.J., 2011. Unstable deformation and the formation of the equatorial bulge of Iapetus. Lunar Planet. Sci. XLII. Abstract 2441.

Dombard, A. J., Cheng, A. F., McKinnon, W. B., and Kay J.P. 2010. The Weirdest Topography in the Outer Solar System: The Ridge on Iapetus and its Possible Formation via Giant Impact. AGU Fall Meeting Abstracts. P31D-01.

Kay, J.P., Kattenhorn, S.A. 2009. Geologically young troughs on Europa: the case for recent tectonic activity. GSA Abstracts with Programs 41, Paper #156-8.

Kay, J.P., Kattenhorn, S.A. 2009. Searching for evidence of active tectonics on Europa. LPSC Abstracts XL, #2454

Kay, J. P., Collins, G. C., Using discharge and precipitation to estimate runoff coefficients on Titan, LPSC XXXIX, #2203, 2008.

Kay, J. P., Collins, G. C. and Patterson, G. W. Comparison of crater classification schemes on Ganymede, LPSC XXXVIII, #2392, 2007.

TEACHING EXPERIENCE

2017 Teaching Assistant, EaES 111 Earth, Energy and Environment, UIC, Chicago, IL
2016 Teaching Assistant, EaES 111 Earth, Energy and Environment, UIC, Chicago, IL
2014 Teaching Assistant, PHYS 116 Energy for future Decision Makers, UIC, Chicago, IL

2013 Teaching Assistant, EaES 484 Planetary Science UIC, Chicago, IL
2011 Teaching Assistant, EaES 111 Earth, Energy and Environment, UIC, Chicago, IL
2007-2008 Teaching Assistant, Introductory Physics Assistant, Wheaton College, Norton, MA
2007 Teaching Assistant, Introductory Astronomy, Wheaton College, Norton, MA

ACADEMIC HONORS, AWARDS, AND FELLOWSHIPS

2013 Illinois Space Grant (ISGC) Fellowship - $10,000
2009 Featherstone Award for Incoming Graduate Students, University of Idaho Geology Department - $3000
2008 Physics and Astronomy Department Award, Wheaton College, Norton, MA.

PROFESSIONAL SERVICE

2012 NASA MSRP Grant Review Panel

MEMBERSHIPS AND AFFILIATIONS

Geological Society of America (2009-present)
American Association of Petroleum Geologists (2012-present)